1	Shelf ecosystems along the U.S. Atlantic Coastal Plain prior to and during the Paleocene-
2	Eocene Thermal Maximum: insights into the stratigraphic architecture
3	Monika Doubrawa <sup>1*</sup> , Peter Stassen <sup>1,2,*</sup> , Marci M. Robinson <sup>3</sup> , Tali L. Babila <sup>4</sup> , James C. Zachos <sup>5</sup>
4	& Robert P. Speijer <sup>1</sup>
5	
6	<sup>1</sup> Department of Earth and Environmental Sciences, KU Leuven, Belgium
7	<sup>2</sup> OD Earth and History of Life, Royal Belgian Institute of Natural Sciences, Belgium
8	<sup>3</sup> U.S. Geological Survey, Florence Bascom Geoscience Center, Reston, Virginia, 20192, USA
9	<sup>4</sup> School of Ocean and Earth Science, University of Southampton, UK
10	<sup>5</sup> Earth and Planetary Sciences, University of California Santa Cruz, Santa Cruz, California, USA
11	
12	Corresponding author: Monika Doubrawa (Monika.Doubrawa@kuleuven.be)
13	*equally contributing authors
14	
15	Key Points
16	Sedimentation rates on the shelf during the Paleocene-Eocene Thermal Maximum (PETM) were
17	site dependent.
18	The pre-onset excursion (POE) partially mimics the PETM.
19	Benthic foraminiferal biogroups during the PETM can support the stratigraphic framework.
20	
21	

#### Abstract

22

23

24

25

26

27

28

29

30

31

32

33

3435

36

37

38

39

40

41

The Paleocene-Eocene Thermal Maximum (PETM) is the most pronounced global warming event of the early Paleogene related to atmospheric CO<sub>2</sub> increases. It is characterized by negative  $\delta^{18}$ O and  $\delta^{13}$ C excursions recorded in sedimentary archives and a transient disruption of the marine biosphere. Sites from the U.S. Atlantic Coastal Plain show an additional small, but distinct  $\delta^{13}$ C excursion below the onset of the PETM, coined the "pre-onset excursion" (POE), mimicking the PETM-forced environmental perturbations. This study focuses on the South Dover Bridge (SDB) core in Maryland, where the Paleocene-Eocene transition is stratigraphically constrained by calcareous nannoplankton and stable isotope data, and in which the POE is well-expressed. The site was situated in a middle neritic marine shelf setting near a major outflow of the paleo-Potomac River system. We generated high-resolution benthic foraminiferal assemblage, stable isotope, trace-metal, grain-size and clay mineralogy data. The resulting stratigraphic subdivision of this Paleocene-Eocene transition is placed within a depth transect across the paleoshelf, highlighting that the PETM sequence is relatively expanded. The geochemical records provide detailed insights into the paleoenvironment, developing from a well-oxygenated water column in latest Paleocene to a PETM-ecosystem under severe biotic stress-conditions, with shifts in food supply and temperature, and under dysoxic bottom waters in a more river-dominated setting. Environmental changes started in the latest Paleocene and culminated atthe onset of the PETM, hinting to an intensifying trigger rather than to an instantaneous event at the Paleocene-Eocene boundary toppling the global system.

42

43

44

45

46

47

48

49

#### Plain language Abstract

The Paleocene-Eocene Thermal Maximum (PETM) is a global short-term warming event, with temperatures increasing 5–8°C. It took place ~56 million years ago and is the most pronounced warming event of the early Paleogene. It is associated with a large injection of greenhouse gases into the atmosphere, causing a negative carbon isotope excursion, recorded in sediments worldwide. Even though the PETM has been studied intensely it is still debated what initially triggered the event, and whether it occurred rapidly, gradually, or stepwise.

- Here we focus on data from the site South Dover Bridge on the U.S. Atlantic Coastal Plain. Our
- data show an additional small, but distinct  $\delta^{13}$ C-excursion before the onset of the PETM ('pre-
- onset excursion', POE). While the connection between the POE and the PETM is still unclear, this
- could point towards a more gradual onset of the warming event.
- 54 The site was situated in a shallow embayment. A nearby river transporting large amounts of
- sediment provided a thick sedimentary sequence, allowing for a high time resolution. The studied
- interval is correlated to sites close-by, revealing a well-preserved, expanded record. We generated
- 57 benthic foraminiferal, stable isotope, grain-size, clay mineralogy, trace element, and
- paleotemperature records providing detailed insights of the changing paleoenvironment.

60

61

### 1 Introduction

- During the early Paleogene, Earth's climate experienced long-term warming, punctuated
- by short-term warming events known as hyperthermals (Bijl et al., 2009; Westerhold et al., 2020;
- Zachos et al., 2008). The most pronounced of these hyperthermals is the Paleocene-Eocene
- 64 Thermal Maximum (PETM, ~56 Ma) which is globally recognized in marine and terrestrial
- sediments by a negative carbon isotope excursion (CIE; Kennett & Stott, 1991; Koch et al., 1992;
- Zachos et al., 2005). The PETM and CIE were caused by a major injection of <sup>13</sup>C-depleted carbon
- into ocean-atmosphere reservoirs, and thus represent a useful deep-time analogue to extreme
- greenhouse driven global warming (Gingerich, 2019; Zeebe et al., 2016; Zeebe & Lourens, 2019).
- 69 Understanding the environmental impact of past climate change on shelf ecosystems can provide
- 70 insights into the effects of future change on today's shallow marine ecosystems (Hollis et al.,
- 71 2019).
- The PETM is characterized by a global ocean temperature increase of 5–8 °C (Kennett &
- 73 Stott, 1991; Sluijs et al., 2006; D. J. Thomas et al., 2002; Zachos et al., 2006). Additionally, the
- 74 PETM is associated with surface ocean acidification (Babila et al., 2016, 2018), shoaling of the
- calcite compensation depth (Zachos et al., 2005), regional changes in the hydrological cycle on
- land, and intensified seasonality (McInerney & Wing, 2011; Rush et al., 2021; Stassen et al., 2015).
- Marine biotic responses to the severe environmental changes are mostly reflected in migration and
- diversification patterns, including organic-walled dinocyst blooms (Sluijs, Bowen, et al., 2007;

Speijer et al., 2012). Deep-sea benthic foraminifera are the only marine group known to have suffered a major extinction at the onset of the PETM (Speijer et al., 2012; E. Thomas, 1998; E. Thomas & Shackleton, 1996).

The majority of marine PETM studies are conducted on deep-sea sediment cores, which generally do not provide the necessary time resolution due to low sedimentation rates. Often these records are also truncated by a dissolution interval just below and within the basal part of the CIE, an important stratigraphic interval needed to unravel subtle changes leading up to the PETM (E. Thomas & Shackleton, 1996; Zachos et al., 2005). The relatively high sedimentation rates on the U.S. Atlantic Coastal Plain cores enable a higher temporal resolution of the Paleocene-Eocene transition, allowing for detailed analyses of the sequence of environmental and biotic changes. Previous studies of sites in New Jersey, such as Wilson Lake (WL) or Bass River (BR, Figure 1A), include various latest Paleocene precursor events, such as pre-PETM warming, sea-level rise and spread of the dinoflagellate *Apectodinium*, as well as changes throughout the CIE, like the appearance of stress-resistant benthic foraminifera, a pH decrease, and strong warming of shallow waters (Babila et al., 2016; Sluijs, Brinkhuis, et al., 2007; Sluijs et al., 2008; Stassen et al., 2015; Zachos et al., 2006).

PETM sedimentary deposits in the Salisbury Embayment (Maryland, Delaware, New Jersey) are marked by the widespread distribution of fine-grained marine sediments, probably related to a regional runoff intensification, contrasting with the Paleocene sediment-starved setting (John et al., 2008; Stassen et al., 2012). Recent stable isotope data from two cores in Maryland show a 1.0–1.5% negative  $\delta^{13}$ C excursion in bulk marine carbonate and foraminifera in a more clayey interval below the onset of the PETM (Babila et al., 2022; Lyons et al., 2019; Self-Trail et al., 2012), coined the POE, or "pre-onset excursion" (Bowen et al., 2015). The stratigraphic significance of the POE is unclear, but similar excursions just below the PETM have been described in bathyal deposits of the Forada section in Northern Italy (Giusberti et al., 2007; Luciani et al., 2007) and the Tasman Sea (Elling et al., 2019), as well as in terrestrial deposits in the Big Horn Basin, Wyoming, USA (Bowen et al., 2015). Pre-PETM environmental changes in form of stratification and increased terrestrial runoff are also reported from expanded Paleocene records from the North Sea Basin. Those changes may be related to increased regional precipitation and major regional uplift, influenced by the North Atlantic Igneous Province (Kender et al., 2012). The

connection of these events and relatively small isotopic excursions to the PETM, as well as to each other, is still unclear, but they could point towards an increasingly unstable carbon cycle and environment during the latest Paleocene leading to a gradual or stepwise change towards the PETM (Bowen et al., 2015; Jones et al., 2019).

In this study we correlate the South Dover Bridge core (SDB, Maryland, USA, Figure 1A) PETM sequence with other cores from Maryland and New Jersey in order to evaluate its stratigraphic completeness and strengthen the existing stratigraphic framework, based on  $\delta^{13}C$  and existing nanno plankton data (Self-Trail et al. 2017). We expand previously published benthic foraminiferal data from SDB (Robinson & Spivey, 2019) across the whole PETM interval and establish a supporting biostratigraphy. Additionally, we suggest time constraints for duration of the latest Paleocene and POE. To determine whether the POE is associated with environmental changes, we examine high-resolution benthic foraminiferal distributions, stable isotope, trace-element, grain-size and clay mineralogy data from the uppermost Paleocene and PETM interval of SDB.

Sedimentation during the PETM is thought to be controlled by the paleo-Potomac Riveroutflow system. This river system, sometimes referred to as the "Appalachian Amazon", carried high volumes of fresh water and sediment onto the shelf (Kopp et al., 2009). As such, the SDB core also provides insight into terrestrial processes.

### 2 Geological and regional setting of the South Dover Bridge core site

The U.S Geological Survey drilled the SDB core in Talbot County, Maryland, USA (Alemán González et al., 2012). During the latest Paleocene and early Eocene, the site was situated in a middle neritic environment on a stable shelf, in proximity of the mouth of the paleo-Potomac River (Robinson & Spivey, 2019; Self-Trail et al., 2012). The northern (New Jersey) part of the embayment has been well studied (e.g., WL and BR), but detailed correlations to the southern part (Maryland, Delaware) are currently lacking.

The uppermost Paleocene in the SDB core is represented by glauconitic quartz sands of the Aquia Formation (Nogan, 1964). In the corresponding  $\delta^{13}C_{bulk}$  record, a pre-onset excursion (POE) of ~2‰ has been described covering the finer-grained interval from 205.9 m to 207 m, (Robinson

& Spivey, 2019; Self-Trail et al., 2012). The silty clay of the PETM, known as the Marlboro Clay, has a sharp lower contact at 203.9 m core depth (Kopp et al., 2009). The onset of the PETM at SDB is characterized by a  $\delta^{13}C_{bulk}$  excursion of -4‰ (Self-Trail et al., 2012) and a dissolution interval, leaving the lowermost meters of the Marlboro Clay nearly barren of calcareous components. The transition from the Marlboro Clay to the Nanjemoy Formation is marked by two unconformities at 188.4 m and 187.1 m, and overlying sediments are more silt-dominated above a sandy interval between the unconformities (Self-Trail et al., 2012). The unconformities truncating the PETM sequence are widespread in the U.S. Atlantic Coastal Plain.

### 2.1. Preservation

Overall, the benthic foraminifera in the Aquia Formation show moderate to good preservation with little to moderate test breakage, dissolution indications and infillings of iron-oxide minerals. Few foraminiferal specimens exhibit a frosty test appearance indicating diagenetic alteration. Only the POE interval, a few meters below the base of the CIE, coincides with a partial dissolution interval. Partially dissolved tests, as well as a high number of broken foraminifera tests make identification to species level difficult to (rarely) impossible.

The lowermost two meters of the Marlboro Clay is nearly completely barren of calcareous foraminifera and other calcareous fragments, while agglutinated specimens become more abundant (Robinson & Spivey, 2019), indicating carbonate dissolution. The cause of carbonate dissolution is thought to be due to a combination of shelf acidification (i.e. pH-decline, carbonate saturation state) and taphonomic alteration (Bralower et al., 2018). Above that interval, the preservation is good to excellent. Foraminiferal specimens are abundant and glassy, with delicate structures preserved.

### 3 Methods

For the foraminiferal study, sediment samples were dried at 45°C for at least 24 hours, weighed, disaggregated with distilled water and washed with tap water over a standard 63  $\mu$ m sieve. The residue was dried at 45°C and weighed to obtain the weight percentage of the >63  $\mu$ m fraction. To obtain insight into the changes in clay content, for selected samples only distilled water was used during this step. The <63  $\mu$ m fraction was captured and dried in the oven. The <2  $\mu$ m fraction underwent Jackson treatment (Jackson, 2005) before being measured with a Philips

PW 1380 diffractometer equipped with CuKalpha radiation, 45kV and 30mA graphite monochromator of the Department of Earth and Environmental Sciences, KU Leuven, and was quantified through Rietveld Refinement for clay content.

167

168

169

170

171

172

173

174

175

176

177

178

179

180

181

182

183

184

185

186

187

188

189

190

191

192

193

194

195

To obtain a more detailed grain-size spectrum, additional measurements were performed on 77 selected samples (every  $\sim$ 33 cm) with a Beckman Coulter LS13 320 Laser Diffraction Particle Size Analyzer of the Department of Earth and Environmental Sciences, KU Leuven. Samples were manually disaggregated, and then treated with HCl and  $H_2O_2$  to remove calcareous components as well as organic matter. For grainsize classification, the international scale ISO 14688-1 was used.

Appropriate splits of those 77 samples (>63 µm, containing ~250–300 benthic foraminifera) were fully counted to obtain a planktic to benthic foraminiferal ratio (planktic/ $(\Sigma)$ planktic+benthic), %P). This ratio may enable estimates of the paleodepth, although effects of taphonomic alteration and changes in bottom-water conditions should not be neglected (van der Zwaan et al., 1990). The %P is also used for correlation between sites. Forty-nine samples were used for a quantitative analysis of the benthic foraminifera. For each sample, a representative split was obtained through an ASC microsplitter. All benthic foraminifera from the split were selected, sorted and mounted on Plummer slides to enable taxonomic counts. For obtaining insight into paleoenvironmental developments and shelf-wide stratigraphic correlations, certain foraminiferal taxa were combined into biogroups (groups of taxa with shared environmental preferences). We used the biogroups defined in Stassen et al. (2012) to allow for a regional comparison across the shelf. These biogroups were established for the PETM interval in New Jersey via cluster analysis and we use them to improve the comparison between the areas. Although the usage and validity of biogroups has been under discussion, we use them to strengthen the stratigraphic framework based on stable isotopes and (partially patchy) nannofossil record. The main two drivers influencing benthic assemblages of such biogroups are oxygen and nutrient levels of bottom and pore waters (van der Zwaan et al., 1999), which often vary on a later scale across a basin. The relative proportions of the biogroups were further used to identify major ecozones in the PETM and to track these zones across the shelf. Comparable biozonation data for the upper Paleocene shelf is currently lacking.

Species of biogroup 1 are *Anomalinoides acutus*, *Pulsiphonina prima* and *Tappanina selmensis* (Figure 1Bc, a, h). Biogroup 2 consists of *Pseudouvigerina* spp. (combining *P. wilcoxensis* and *P. triangularis*) and *Spiroplectinella laevis* (Figure 1Bg, e). Biogroup 3 includes *Turrilina brevispira* (Figure 1Bd) and *Bulimina callahani*, but the latter is not present in the assemblages at SDB. Biogroup 1 is characteristic of continuously stressed conditions whereas biogroup 2 is characteristic of periodically stressed with dysoxic bottom water conditions (Gibson et al., 1993; Rostami et al., 2020; Self-Trail et al., 2017; Stassen et al., 2015). Species in biogroup 3, while also tolerant of stressful environments, are more characteristic of well-oxygenated, eutrophic conditions (Ernst et al., 2006; Stassen et al., 2015) and are more abundant at greater paleodepths (middle to outer neritic). For further taxonomic and environmental discussions of the biogroups we refer to Stassen et al. (2012, 2015) and the Supporting Information Text S1 and Figure S1.

Cibicidoides alleni (Paleocene) and Anomalinoides acutus (PETM) were used for geochemical analyses (Figure 1Bb, c). Both are epibenthic foraminifera, which exhibit no interspecies stable isotope offset to each other and precipitate the calcite in near equilibrium with the surrounding water (e.g. Lynch-Stieglitz et al., 1999; Stassen et al., 2009). In samples where both species were sufficiently present, both were used for measurements to verify this finding for SDB (Figures 2 & 3). Single-species stable isotope measurements were performed to validate trends of existing  $\delta^{13}C_{\text{bulk}}$  and  $\delta^{18}O_{\text{bulk}}$  carbonate records for the uppermost Paleocene and PETM segments. Cibicidoides alleni and A. acutus were picked from 130 washed samples (5–20 specimens per sample), resulting in an average sample spacing of ~17 cm. Samples were analyzed at the University of California, Santa Cruz with a Kiel Mat 253 gas source mass spectrometer system. All carbon isotope values are given in  $\delta^{13}C$  notation, relative to the PeeDee belemnite Standard (PDB), with an analytical error of  $\delta^{13}C$ :  $\pm 0.05\%$  and  $\delta^{18}O$ :  $\pm 0.08\%$ .

Additional benthic foraminifera (*C. alleni, A. acutus*) from the 180–250 µm size fraction were picked, crushed and cleaned with a multi-step oxidative and reductive cleaning treatment (Boyle & Keigwin, 1985; later modified in Rosenthal et al., 1997). Trace elemental analyses were carried out at the University of California, Santa Cruz on a Thermo Scientific Element XR Sector Field Inductively Coupled Plasma Mass Spectrometer (SF-ICP-MS). Based on repeated analysis of laboratory consistency standards throughout the length of the study, analytical reproducibility on

227

228

229

230

231

232

233

234

235

236

237

238

239

240

241

242

243

244

245

246

247

248

249

250

251

252

253

Mg/Ca is 2% (2SD). For all stable isotope and trace element measurements, only well-preserved specimens were chosen (Figure 1Bi, j).  $\delta^{18}$ O derived temperature calculations are based on Marchitto et al. (2014) and Lynch-Stieglitz et al. (1999), based on modern calibration of Cibicidoides species. By applying a quadratic temperature dependence, this results in a -0.19‰ per °C in warm waters with the inferred oxygen isotopic seawater composition as a less constrained parameter for deep-time reconstructions in a greenhouse world. The Mg/Ca temperature calibration is also genus-specific and when used in paired measurements with the  $\delta^{18}$ O data, it allows for the deconvolution of the seawater composition and the temperature effects of the measured for aminiferal  $\delta^{18}$ O. Deep-time application of Mg/Ca paleothermometry requires additional non-thermal consideration of secular variation of seawater Mg/Ca (Mg/Ca<sub>sw</sub>) on the Mg distribution coefficient and Mg/Ca-BWT (bottom water temperature) proxy sensitivity. The Mg/Ca-BWT calibration of Lear et al. (2002) based on recent Cibicidoides spp. and spanning the largest temperature range (up to 18°C) was primarily used to reconstruct BWT (e.g., de Bar et al., 2019) and an additional power correction scheme was used to account for the influence of lower Mg/Ca<sub>sw</sub> on Paleogene ocean temperature estimates (Evans & Müller, 2012). To address speciesspecific calibration constants and the power component, which relates to the sensitivity of the calibration of the Mg content of the Eocene ocean, the SDB Mg/Ca derived BWT calculations follow Hines et al. (2017), basing their Eocene calculations on multiproxy data comparison and a predetermined Paleogene Mg/Casw value of 1.6 mmol/mol. Diagenetic screening was done by microscopy, including SEM imagery and utilizing Sr/Ca as main geochemical indicator (Kozdon et al., 2013). Except for one sample (209.01 m) all benthic Sr/Ca values were greater than 1.0 mmol/mol, and thus fall into the reported range of modern Cibicidoides spp. (Rosenthal et al., 1997). Bottom water temperatures are likely >3°C and the paleodepth of SDB was well above the calcium carbonate compensation depth and we therefore did not apply any carbonate ion correction to Mg/Ca-derived temperatures. No salinity correction of the Mg/Ca values is applied (Hollis et al., 2019) as no independent data is available to verify salinity variations of the sea floor at this site, although alterations in the hydrological cycle are expected during the PETM, resulting in reduced uptake of Mg in the test wall.

### 4 Results

### 4.1. $\delta^{13}C_{carb}$ records

Latest Paleocene  $\delta^{13}$ C records commonly exhibit a consistent pattern leading up to the PETM. This pattern is especially known from deep-sea sites with very low sedimentation rates (<5 mm/kyr) where short-lived events. In several shallow marine and terrestrial sequences,  $\delta^{13}$ C<sub>carb</sub> excursions of ~-2‰ have been detected just below the PETM (e.g., CamDor, USA, Forada, Italy, Big Horn Basin, Wyoming; Babila et al., 2022; Bowen et al., 2015; Giusberti et al., 2007; Lyons et al., 2019). The  $\delta^{13}$ C<sub>bulk</sub> record of SDB displays a ~-2‰ excursion in the uppermost Paleocene (Self-Trail et al., 2012, 2017). Our benthic foraminiferal  $\delta^{13}$ C record closely follows the  $\delta^{13}$ C<sub>bulk</sub> record (Figure 2), with uppermost Paleocene pre-POE  $\delta^{13}$ C<sub>benthic</sub> values centering around 1‰. In the more fine-grained POE interval at 207 m, the values shift to ~-1‰, becoming more positive again in the interval between the top of the POE (205.7 m) and the base of the Marlboro Clay (204 m), though not completely returning to pre-POE values.

The onset of the CIE at SDB is within a carbonate-poor interval and is marked by an abrupt decrease of  $\delta^{13}C_{benthic}$ . The interval 204–203 m is barren of calcareous foraminifera (likely due to dissolution; Robinson & Spivey, 2019), thus it does not provide information on the basal part of the PETM. The  $\delta^{13}C_{bulk}$  record is also unreliable for this interval. The  $\delta^{13}C_{benthic}$  values shift to ~3‰, plateau at 196.9 m, then start to gradually increase until the unconformity at 189 m. Above the unconformity at the base of the Nanjemoy Formation, mean values are lower than the regional Paleocene average (Figure 2).

### 4.2. Grain-size distributions

The upper Paleocene glauconitic Aquia Formation is generally dominated by the fine sand fraction (Figure 3), but at 207.5 m, just below the POE, the proportions of the finer fractions (mostly clay and fine silt) abruptly increase, at the expense of the sand fraction. Above the POE, the sand fraction briefly returns in the grain-size suite, which shifts to a coarser mean grain-size before gradually changing to the clay and fine silt dominated suite at the base of the PETM (Figure 3). The fine-grained composition remains dominant up to ~193 m, from whereon the medium to coarse silt fraction of the Marlboro Clay increases.

At SDB the clay suite of the Aquia Formation consists mostly of illite, smectite and fine-grained glauconite, with only small proportions of kaolinite (<5%). No mineralogical changes in the clay composition are observed in the clay-enriched POE level. In the uppermost Paleocene, at the transition to the Marlboro Clay, the kaolinite content increases to a maximum of 30%, parallel to the overall decrease in grain-size, reaching up to 40% in the dissolution interval at the base of the PETM (Figure 3). It gradually decreases throughout the CIE towards ~15% at the unconformity at 188.4 m, as also observed in other sites (Gibson et al., 1993, 2000; John et al., 2012).

### 4.3. Foraminifera: relative abundance of planktics & benthic biogroups

The %P in the uppermost Paleocene interval at SDB is low (<5–10%, Figure 2). At 205.5 m the %P nearly doubles. Above the dissolution interval marking the basal part of the PETM, the %P rises to up to 60%, up to 198 m, where it drops to 20–30% and finally to 10–20% from 192 m upwards, including the lower part of the Nanjemoy Formation.

At SDB, biogroup 2 is well represented (~15%) in the uppermost Paleocene, temporarily increasing at the base of the POE to 25%, and from there gradually decreasing towards the onset of the PETM (Figure 4). Biogroups 1 and 3 both have low abundances (<5%) in the Aquia Formation. In the POE interval, Biogroup 1 is represented by a small spike of 10% in one single sample (5% of both *Pulsiphonina prima* and *Anomalinoides acutus*, Figure 4). Biogroup 3 is an insignificant component of the Paleocene assemblage at SDB and vanishes from the record during the PETM.

Biogroup 1 has high occurrences throughout the Marlboro Clay, mainly represented by *Pulsiphonina prima* and *Anomalinoides acutus* (rare *Tappanina selmensis*). Abundances are above 70% at the onset of the PETM but decrease to 30% twice throughout the following interval (from 197.8 m upwards and from 194 m upwards), which is within a gradual decreasing trend towards the top of the PETM interval. Similar patterns as in biogroup 1 can be observed in the %P, with larger abundances above the dissolution interval and values around 20% throughout the recovery phase. Biogroup 2 increases in abundance above the dissolution interval from <5% to a maximum of 25% between 200 m and 196.5 m, where its abundance rapidly decreases to ≤10% for the upper part of the studied interval.

# 4.4 $\delta^{18}$ O and Mg/Ca: Temperature and $\Delta$ salinity

Benthic foraminiferal  $\delta^{18}$ O records were generated for two species, *Cibicidoides alleni* (Paleocene) and *Anomalinoides acutus* (Eocene). Over the uppermost Paleocene prior to the CIE,  $\delta^{18}$ O values gradually decrease by 0.5% (Figure 3), then abruptly decline to <-3.0% at the onset. Through the remainder of the CIE, values gradually increase, nearly reaching pre-PETM values beneath the unconformity at the top of the Marlboro Clay. A lower resolution benthic foraminiferal Mg/Ca record was generated using just *C. alleni*. Upper Paleocene values are generally low, ~3.3 mmol/mol, with a few higher values recorded just below and above the POE interval (Figure 3). At the onset of the CIE, the Mg/Ca content rises to a maximum of 5.5 mmol/mol. From 197 m upwards, a decreasing trend is observed, gradually shifting back towards uppermost Paleocene values, reaching 2.5 to 3 mmol/mol at the base of the Nanjemoy Formation.

We based our Paleocene  $\delta^{18}O_{sw}$  estimate on the average value of sample-depths where we could couple Mg/Ca-temperatures (according to Hines et al., 2017) with foraminiferal  $\delta^{18}O$  (n=9). The result is a latest Paleocene average  $\delta^{18}O_{sw}$  of -0.65% (SD 0.36), in accordance with other studies in this region (e.g., Zachos et al., 2006). For regional variations in  $\delta^{18}O_{sw}$  during the PETM, we simply derived a linear trend based on the coupling with the Mg/Ca data (Figure 3). The lowest  $\delta^{18}O_{sw}$  (<-2%  $\pm 0.34$ ) was obtained in the initial phase of the PETM, with values increasing (>-1.5%) in the recovery phase. This computation does not take into account the potential influence of changes in carbonate saturation on benthic Mg/Ca and variations in local salinity.

The benthic  $\delta^{18}O$  and Mg/Ca indicate an average latest Paleocene bottom water (~120 m paleodepth; Robinson & Spivey, 2019) temperature of ~17.7°C (mean Mg/Ca: 17.8 °C ± 1.9 °C; error includes analytical, sample and standard calibration error (Hines et al. 2017). The benthic  $\delta^{18}O$  indicates a slow shift towards warmer conditions in the latest Paleocene with no change during the POE.

The inferred change in temperature based on  $\delta^{18}O$ , considering a fixed  $\delta^{18}O_{sw}$  of -1.2‰ for the PETM interval, exceeds that based on Mg/Ca, raising the possibility that  $\Delta\delta^{18}O_{benthic}$  was strongly amplified by a reduction in local  $\delta^{18}O_{sw}$ . For the post-POE and PETM,  $\delta^{18}O$ -based temperatures, using a Mg/Ca- $\delta^{18}O$  coupled estimate of  $\delta^{18}O_{sw}$ , show an accelerated shift prior to the onset of the CIE, to 18–20 °C, reaching up to 22 °C above the dissolution interval during peak PETM warming. Mg/Ca-based temperatures show a wider scatter in the latest Paleocene, but in

the PETM show a distinct warming trend consistent with the  $\delta^{18}O$  decrease. Temperatures remain high (19–22 °C) up until 196 m, from whereon they gradually decrease, reaching bottom water temperatures of 16–17 °C in the upper part of the Marlboro Clay. Overall, we infer bottom water warming of minimal 5°C between the base of the POE and peak warming of the PETM. The inferred change in temperature based on  $\delta^{18}O$  exceeds that based on Mg/Ca, raising the possibility that  $\Delta\delta^{18}O_{benthic}$  was amplified by a reduction in local  $\delta^{18}O$  seawater ( $\delta^{18}O_{sw}$ ).

## Regional stratigraphy

### 5.1. Bio-, chemo-, and lithostratigraphic correlation

To enable a basin-wide stratigraphic correlation along the depth gradient (Figure 2), we combined chemostratigraphic ( $\delta^{13}$ C), lithostratigraphic and biostratigraphic (calcareous nannofossils) data with environmental proxies (%sand fraction and %P) as previously established for the New Jersey sites (Stassen et al., 2012). The POE at SDB is characterized by a  $\delta^{13}$ C<sub>benthic</sub> shift of -2‰, as well as a consistent and modest decrease in grain-size (Figure 2) just below the lowest consistent occurrence (LCO) of the calcareous nannofossil *Hornibrookina arca*. The %P is low up to the top of the POE, where it increases. These characteristics evident in the POE at SDB are only partially traceable across the shelf in Maryland (e.g., CamDor site; Bralower et al., 2018). In the available  $\delta^{13}$ C<sub>bulk</sub> and  $\delta^{13}$ C<sub>benthic</sub> records, there is no clear evidence of a negative carbon isotope excursion prior to the CIE in any of the New Jersey sites (Figure 2). The grain-size data for WL and BR, though, show a similar trend towards finer grain-sizes in the uppermost Paleocene, and these intervals are also positioned below the LCO of *H. arca*, but no further stratigraphic tie points are available. The resolution of the stratigraphic data from the Millville and Ancora cores is too low to be able to detect a clear change. Above the potential POE at BR (~457.5–357.75 m) and WL (~110.8–110.2 m), the %P increases slightly, as also observed at SDB.

The CIE is commonly divided into a core phase and a recovery phase (Röhl et al., 2007). Several calcareous nannofossil marker taxa are associated with the PETM, for instance the lowest occurrence (LO) of *Discoaster anartios* (base NP9b) and *Tribrachiatus bramlettei* (base NP10). The CIE core phase is defined as starting from the initial decrease of  $\delta^{13}$ C values, followed by an interval of sustained low  $\delta^{13}$ C values until they begin to increase again, around the NP9/NP10 boundary (Röhl et al., 2007; Self-Trail et al., 2012, 2017). In Maryland, the CIE onset coincides with the transition from the sandy Aquia Formation (correlating with the Vincentown Formation

in New Jersey) to the silty-clayey Marlboro Clay. Both can be clearly traced from the New Jersey sites (BR, Millville, Ancora and WL) to SDB and are supported by biostratigraphic correlations (see Figure 2).

370

371

372

373

374

375

376

377

378

379

380

381

382

383

384

385

386

387

388

389

390

391

392

393

394

395

396

397

398

399

400

The negative CIE to ~-3\% at the onset of the PETM at SDB is similar to the general pattern observed in other Maryland and New Jersey sites (Figure 2). The CIE recovery phases are characterized by trends observed in deep-sea records. In the U.S. Atlantic Coastal Plain, high but discontinuous sedimentation rates during the PETM (Figure 5B; Gibson et al., 2000; Kopp et al., 2009; Stassen et al., 2012) may distort trends in the CIE recovery phases. Therefore, the position of the CIE recovery phases are based on the relative magnitude of the recovery correlated with ODP Site 690 (Figure 5A; Bains et al., 1999). We assume that there is no acceleration or delay of the carbon isotope recovery along the shelf due to local differences in paleoproductivity or river outflow. We developed a percentage recovery metric that scales between late Paleocene and CIE core phase  $\delta^{13}$ C values, such that the core phase is 0% (no recovery) and a return to late Paleocene δ<sup>13</sup>C values represents 100% (full recovery). Thus for each site, Paleocene background values (excluding POE intervals) were used to estimate the position of a 100% recovery of the CIE. The 0% calibration level is the average value of the CIE core phase. To avoid circular reasoning, the δ<sup>13</sup>C<sub>benthic</sub> values between the two major %P peaks were chosen to define CIE core values; the lower one (line a in Figure 2) is situated above the base of the CIE, and the higher one is within the core phase (line c). For the Millville site, the Paleocene values are based on Gavelinella beccariiformis, a species known to yield results with a constant offset relative to A. acutus or C. alleni, which we adjusted for by the correction factor 1.12% (Stassen, 2012; Stassen et al., 2009). For the recovery calculations, we based the  $\delta^{13}C_{benthic}$  values of the core phase on an estimated interval, as no clear plankton peaks can be discerned in the Millville record (272.6–267.8 m).

The %P in the CIE core phase of SDB shows two distinct peaks and two lows, which are also observed at WL and BR (correlation lines a to c in Figure 2). At both SDB and WL, the LO of *Tribrachiatus bramlettei* (base NP10a) occurs just below the lower %P-minimum (line b), and the LO of *Phthanoperidium crenulatum* below the second %P-maximum, supporting the stratigraphic significance of these correlations across this shelf. The lower part of the Marlboro Clay also contains the stratigraphic marker taxa *Tribrachiatus bramlettei* marking the base of NP10, separating it from NP9b where the PETM excursion taxon *Discoaster anortios* is already present (Self-Trail et al., 2012). At Millville, the preservation of nannoplankton is reported as bad

to mediocre, thus its NP-zonation is not straightforward. *Discoaster anartios* is present at three sites: at Millville (275 m), SDB (LO at 200.5 m; Self-Trail et al., 2012) and Ancora (LO at 169.77 m). At all sites, the taxon appears just below the lower %P minimum (line b, Figure 2).

The recovery phase starts at ~196.9 m core depth at SDB, a level ~7 m above the PETM onset, from where the  $\delta^{13}$ C<sub>benthic</sub> values gradually return to more positive values (Figures 2 and 5A). At Ancora, a distinct transition to quickly increasing  $\delta^{13}C_{benthic}$  values from the 0% mark is observed at ~165.8 m, while at BR the start of the recovery is less sharp and located around ~353 m (Cramer & Kent, 2005; Stassen et al., 2012). At WL, only the CIE core phase is present (Stassen et al., 2012). The CIE recovery can be further divided into phase 1, with a slow increase of  $\delta^{13}$ C, and phase 2, where the isotope curve steepens. In recovery phase 2 at ODP Site 690, the  $\delta^{13}$ C values shift from the 0–25% recovery of phase 1 to values  $\geq$ 50%. At SDB,  $\delta^{13}$ C<sub>benthic</sub> values cross the 25% recovery boundary at 192 m, to which we extrapolate the boundary between CIE recovery phase 1 and 2. Additionally, based on the relative position of the LO of D. anartios, the  $\delta^{13}$ C<sub>benthic</sub> values and the relative recovery magnitude, we moved the boundary between the CIE core and the recovery phase at Millville from ~264 m (Makarova et al., 2017) to ~267 m. At BR the base of phase 2 is accompanied by a significant decrease in the %P, a similar pattern as observed at SDB. Additionally, the highest occurrence of D. anartios is situated in recovery phase 1 at BR, correlating with the highest occurrence at SDB (193.9 m, Cramer et al., 1999). Recovery phase 2 is truncated by an overlying unconformity at 188.6 m (Self-Trail et al., 2012), and most of recovery phase 2 seems to be missing at SDB.

### 5.2. Ecostratigraphy based on PETM ecozones

401

402

403

404

405

406

407

408

409

410

411

412

413

414

415

416

417

418

419

420

421

422

423

424

425

426

427

428

429

430

In order to support the calcareous nannofossil and  $\delta^{13}C_{carb}$  stratigraphy, three benthic biogroups were used for basin-wide correlation with sites in New Jersey. Their distributions reflect systematic patterns in a stratigraphic sequence of disruptions of the benthic ecosystem during the PETM (Stassen et al., 2012, 2015). Therefore, ecozones based on the abundance patterns of these biogroups are used under the assumption of a near synchronous duration on a regional scale, reflecting environmental changes that influenced the shelf to a broad extent during the PETM. The boundaries of the ecozones are based on changes of the most dominant group in each interval.

In the uppermost Paleocene of the Southern Maryland region, the taxa of these biogroups are rare. The main taxa of the SDB Aquia Formation, which are not included in any of the typical

PETM-biogroups (Figure 4), indicate stable, oxygenated, eutrophic bottom water conditions during the latest Paleocene and include *Bulimina virginiana*, *Paralabamina lunata*, or an assemblage of *Cibicidoides* species (*C. alleni, C. howelli, C. marylandicus, C. irenae, C. succedens*, Figure 1Bb, i). The corresponding %P in the upper Aquia Formation is low but increases towards the base of the PETM, a change attributed to a regional sea-level rise (Gibson et al., 1993; Robinson & Spivey, 2019). A similar pattern is observed in the Vincentown Formation at BR. Planktic foraminifera appear at a similar stratigraphic level at WL (Stassen et al., 2015).

Biogroup 2 taxa, able to cope with periodically stressed dysoxic bottom water conditions, occur with ~10% abundance, and increase to ~20% at 207 m, at the base of the POE, then gradually decrease towards the base of the PETM. A taphonomic bias causing this decline cannot be fully excluded, as it coincides with a strong decrease of *B. virginiana*, a thin-shelled, small species, which is presumably susceptible to dissolution (Nguyen et al., 2009). The fining trend in the sediment and the increased dissolution detected during the POE interval do mimic some PETM characteristics (Babila et al., 2022), but no distinct kaolinite influx is recorded. Attributing the pre-PETM abundance increase of biogroup 2 to specific environmental changes is thus not straightforward.

The basal meter of the PETM interval is barren of calcareous components and thus cannot be resolved based on foraminiferal proxies. A transition interval with a gradual grain-size decrease and biotic turnover, as detected at WL, is a possibility, but clear evidence is missing. The %P strongly increases above the dissolution interval, a pattern which is observed all over the U.S. Atlantic Coastal Plain and may be attributed to a significant rise in sea-level, but this interpretation could be biased by better preservation of planktic foraminifera.

Parallel to the increase in %P in the lower part (above the dissolution interval) of the PETM interval, biogroup 1 appears as the most dominant benthic group, increasing to 90% of the total benthic foraminiferal assemblage. *Pulsiphonina prima*, *Anomalinoides acutus* and *Tappanina selmensis* are thought to have flourished in continuously stressed dysoxic bottom water conditions and with transient food supply (Figure 1Ba, c, h). During the PETM, the hydrological cycle was likely intensified (Kopp et al., 2009; Rush et al., 2021), leading not only to higher sediment input to the shelf, but also to stratification of the water column due to fresh-water input by the nearby

paleo-Potomac River, causing possible anoxia to hypoxia in the bottom waters. These circumstances allowed biogroup 1 to become strongly dominant, marking the start of the PETM ecozone A that can be recognized on a regional scale (Figure 4).

Biogroup 2 is subordinate in the basal part of the CIE core phase, but above 201 m it increases, reaching 20% at 199 m. This significant abundance increase marks the transition to PETM ecozone B and indicates an improvement in bottom water conditions, with increased oxygen levels (Stassen et al., 2012, 2015), and a potential return to episodic influences of major river outflow in the basin. The lower boundary of ecozone B precedes the reduction of kaolinite abundance in the PETM clay in the lower part of NP10 in New Jersey (Cramer et al., 1999; Gibson et al., 2000). The resolution of kaolinite-estimates at SDB is relatively low, but the data support the positioning of the ecozonal boundary, as a decline in kaolinite probably occurs above 199 m (Figure 3). The transition to ecozone B at all sites takes place in the core phase of the CIE (Figure 6, arrows B). The seemingly belated transition at Millville is likely due to the low resolution of assemblage data, which only allows for only a rough estimation of the position of biotic changes (Figure 4).

At the deeper sites of Ancora, Millville and BR in New Jersey, biogroup 3 is consistently present in recovery phase 2 of the CIE. Its abundance increases opposed to PETM biogroup 1 and 2, and is associated with the establishment of eutrophic, yet oxic conditions at the seafloor (Ernst et al., 2006; Stassen et al., 2015). In contrast, biogroup 3 does not occur in the Marlboro Clay at SDB, and neither does the related stratigraphic ecozone C. *Bulimina callahani* is absent at SDB, hinting towards an absence of ecozone C compared to deeper sites in New Jersey, although the upper part of the CIE recovery is truncated at SDB. *Turrilina brevispira* occurs only rarely in the uppermost Paleocene sediments. Both taxa are associated with deeper environments (Speijer & Schmitz, 1998; Speijer & Wagner, 2002; Stassen et al., 2015), the shallower paleodepth at SDB and WL has therefore likely an additional influence on their absence. Nevertheless, at all three New Jersey sites, the base of ecozone C is just below or coincides with the base of isotope recovery phase 2 (Figure 6, arrows C). This supports our interpretation that the final recovery phase of the CIE is not fully present at SDB and that parts are eroded (Figures 4 and 6), a phenomenon observed at many sites in this region.

### 5.3. Sedimentation rates across the shelf

490

491

492

493

494

495

496

497

498499

500

501

502

503

504

505

506

507

508

509

510

511

512

513

514

515

516

517

518

519

Given the short interval of recovered Paleocene, the usual upper Paleocene tie points, e.g., the base of magnetochron C24r at BR (Cramer et al., 1999), or the LO of *Discoaster multiradiatus*, indicating base NP9a at Ancora (Miller, 1999) and BR (Cramer et al., 1999), are not recorded at SDB (Self-Trail, 2011). As such, estimates of latest Paleocene sedimentation rates at SDB are based on extrapolation of estimates from New Jersey sites. Latest Paleocene sedimentation rates for Maryland and New Jersey are relatively low, between 0.1 to 1.0 cm/kyr, indicating a sediment starved setting (Gibson & Bybell, 1991; Stassen et al., 2012, Table 1). Similarly, the latest Paleocene linear sedimentation rate at SDB has been estimated to range from 0.5–2.2 cm/kyr (Lyons et al., 2019). As Millville's microfossil record does not provide any reliable tie-points, we presumed a rate of 1 cm/kyr for the upper Paleocene based on the closest site, BR.

We recomputed rates using the lowest common occurrence (LCO) of *Hornibrookina arca* as a tie-point to link SDB with the New Jersey sites. At BR, where a steady Paleocene sedimentation rate of 1.0 cm/kyr was suggested (Stassen et al., 2012), this LCO is at 0.34 m below the base of the PETM (Gibbs et al., 2006). Assuming a linear correlation between BR and SDB (LCO H. arca: 0.8 m below the base), results in an extrapolated latest Paleocene sedimentation rate of ~2.4 cm/kyr for SDB. In contrast, the lowest occurrences of *Calciosolenia aperta* have been reported from SDB (206.0 m; Self-Trail, 2011) and BR (359.24 m; Gibbs et al., 2006). Using the same assumptions as for H. arca, this would suggest a sedimentation rate of  $\sim 1.03$  cm/kyr for SDB. If we choose to use *H. arca* as the more reliable tie-point and an assumed sedimentation rate of 2.4 cm/kyr, this results in an estimated duration of ~45 kyr for the POE and a duration between the upper boundary of the POE and the PETM of ~80 kyr (Figure 5B). Both sharply contrast with ~2 kyr durations estimated in the Bighorn Basin (Bowen et al., 2015). A doubling of the sedimentation rate for the finer grained POE interval, to mimic the higher sedimentation rates and reduction of grainsize during the PETM (John et al., 2008; Stassen et al., 2012), would shorten the POE to ~22 kyr, putting its onset at ~100kyr before the PETM onset (Figure 6, grey inset box). Admittedly, given the episodic nature of deposition on the shelf and low resolution age constraints, application of long-term average rates to estimate the duration of short-lived or transient events introduces large uncertainties (see Babila et al., 2022), as a short-lasting event, like the POE, are not likely to be captured, but only in a few sites along the shelf (Trampush & Hajek, 2017). Taking

the uncertainties of the respective age models of the POE at SDB and at the Bighorn Basin into account, it is currently not possible to determine whether it concerns the same event in the two areas.

Even with the uncertainties in the latest Paleocene sedimentation rates, it is evident that rates substantially increase during the PETM along the U.S. Atlantic Coastal Plain. Age tie points from the SDB core suggest sedimentation rates of 4.8 to >20 cm/kyr throughout the CIE. This likely is a consequence of a more energetic hydrological cycle enhancing sediment transport and the deposition of the Marlboro Clay over a wide area in the Salisbury Embayment (Gibson et al., 2000; Rush et al., 2021). Our proposed correlation schemes (Figures 2 & 4) indicate that accordingly, SDB has one of the most extensive CIE intervals in the area (15.6 m), similar to the nearby Maryland site CamDor (13.8 m, Lyons et al., 2019) and New Jersey's Millville site (15.8 m, Makarova et al., 2017).

The CIE has well-calibrated chronostratigraphic tie points in  $\delta^{13}$ C records in terrestrial and marine sequences (e.g., Röhl et al., 2007; Zachos et al., 2005). The exact age of the tie points might vary depending on the chosen calibration, e.g., cyclostratigraphy (Röhl et al., 2007) or  $^3$ He (Murphy et al., 2010), but they can be continuously adjusted to more refined age models, as the relative distances in our proposed stratigraphic framework are constant. The age model of Röhl et al. (2007) was used to allow for a straight forward comparison with the results of Stassen et al. (2012) ( $^3$ He-based data are included in brackets in Table 1 for comparison). The selected tie points and ages relative to the base of the CIE for our calculations of sedimentation rates are: the base of CIE recovery phase 1 (71.25 kyr), base of recovery phase 2 (94.23 kyr) and a total CIE duration of 170 kyr (Röhl et al., 2007). Additional marker points are the LO of *T. bramlettei* (~26 kyr) and a regional change in sedimentary regime shortly below the transition from ecozone A to B, which while not detectable at SDB (~35 kyr, see Stassen et al., 2012), has been used for the northern sites.

The sedimentation rate in the CIE core phase at SDB is considerably higher than during the late Paleocene and is consistent with the New Jersey sites. With a sedimentation rate of  $\sim$ 14 cm/kyr (based on the extrapolated regional change in sedimentary regime or  $\sim$ 13.5 cm/kyr, if based on the LO of *T. bramlettei*), it is similar to the rate at WL and Ancora (Table 1). Towards the start of CIE recovery phase 1, the sedimentation rate is reduced to  $\sim$ 6.9–8.0 cm/kyr, depending on

whether the regional change in sedimentary regime or the LO of *T. bramlettei* is used as the base for the calculation, respectively. The same trend is observed at Ancora, where the sedimentation rate changes from 11.2 to 4.3 cm/kyr. In contrast, BR, the most downdip New Jersey site, sees a relative uptake in sedimentation rate from 2.8 to 10.4 cm/kyr during that phase. CIE recovery phase 1 at SDB shows an increase in sedimentation to ~21.3 cm/kyr, the highest for the studied interval, similar to BR (17.2 cm/kyr), and thus the most expanded CIE recovery interval known from this region. Only the lowest part of CIE recovery phase 2 is recorded at SDB, if it is not fully missing due to the overlying unconformity. The  $\delta^{13}C_{benthic}$  values do not return to latest Paleocene levels and exhibit a sharp jump above 188.4 m. If it is assumed that the sedimentation rate of recovery phase 1 (21.3 cm/kyr) persisted unchanged during recovery phase 2, then ~115 kyr of the total duration of the CIE is recorded in the Marlboro Clay at SDB.

Table 1: Comparison of proposed sedimentation rates at SDB and those of the New Jersey sites (Stassen et al.,
 2012). Age tie points based on Röhl et al. (2007) and Murphy et al. (2010) in brackets.

Upper tie point	SDB	Wilson	Ancora	Millville	Bass River
		Lake			
End Paleocene	~1.0–2.4	0.1 cm/kyr	0.8 cm/kyr	-	1.0 cm/kyr
0 kyr	cm/kyr				
regional change in	16.7 cm/kyr	16.9 cm/kyr	11.2 cm/kyr	-	2.8 cm/kyr
sedimentary regime					
35 kyr					
Start CIE recovery 1	8 cm/kyr	22.0 cm/kyr	4.3 cm/kyr	6.3 cm/kyr	10.4 cm/kyr
71.25 kyr (134 kyr)	(6.5 cm/kyr)	(12.0	(5.0 cm/kyr)	(5.6 cm/kyr)	(3.5 cm/kyr)
		cm/kyr)			
Start CIE recovery 2	21.3 cm/kyr	missing	1.3 cm/kyr	15.8 cm/kyr	17.2 cm/kyr
94.23 kyr (167 kyr)	(12.7		(1.2 cm/kyr)	(16.7	(12.7
	cm/kyr)			cm/kyr)	cm/kyr)
CIE end	truncated	truncated	minimum	truncated	truncated
170 kyr (217)			8.4 cm/kyr		
			(12 cm/kyr)		

Estimation of	~115 kyr	~70 kyr	~170 kyr	~111 kyr	~105 kyr
preserved CIE	=~68%	=~41%	=~100%	= ~65%	= ~62%
interval			assumed		

## 5.4. Sedimentary regime in the Salisbury Embayment

The Aquia Formation consists of bioturbated glauconitic sands interbedded with occasional thin clay-layers which were deposited on a shallow shelf (Nogan, 1964; Robinson & Spivey, 2019). The enigmatic ~1 m thick POE interval differs in being more clayey and has so far only been recorded at two sites along this shelf, SDB and CamDor (Bralower et al., 2018; Robinson & Spivey, 2019). The sand content is reduced by ~20% (Figure 3). The fine sand proportion gradually decreases towards the base of the PETM. The fine-grained character of the overlying Marlboro Clay has been attributed to increased river input during the PETM and has been interpreted as a delta-front hyperpycnal flow deposit at the site of the Mattawoman Creek-Billingsley Road core situated closer to the mouth of the paleo-Potomac River (Robinson & Spivey, 2019; Self-Trail et al., 2017).

The changes in proportions of coarse- to fine-grained sediments in the POE are not as strong as at the base of the Marlboro Clay. The clay suite in the POE interval has a low kaolinite percentage (<5%), while it reaches up to 40% in the CIE core phase of the Marlboro Clay, indicating a different clay mineral source(s). The kaolinite of the Marlboro Clay was eroded from the hinterland, transported to the shelf and redeposited, where it diluted the dominant illite/smectite composition (Bornemann et al., 2014; John et al., 2012). While the source of the clay differs, the silt of the POE may have undergone the same transport mechanism, through increased river discharge and hyperpycnal flow. Both sedimentary systems hint towards more vigorous hydrological regimes with episodes of increased runoff (Rush et al., 2021; Stassen et al., 2015). A reorganization of a local distributary system during the POE may explain its limited expression in the sedimentary record, while during the PETM a regional system change occurred, influenced the lateral distribution of fine sediments on a large scale. The varying clay content excludes downmixing from the PETM as the source for the POE-silt.

# 5.5. Magnitude of the PETM $\delta^{13}$ C excursion

The cause of the PETM and the related environmental changes have been ascribed to one or more major injections of isotopically light carbon into the atmosphere-ocean reservoirs, leading to a negative  $\delta^{13}C$  excursion recorded worldwide. The magnitude of the excursion differs between depositional settings and ranges from ~2.5‰ in the deep sea to ~6‰ in terrestrial sequences (Bowen et al., 2015; Röhl et al., 2007). For the shallow U.S. Atlantic Coastal Plain, a regional average  $\delta^{13}C$  excursion of ~4‰ is observed in benthic foraminifera (Stassen et al., 2012; Zachos et al., 2006), with a similar signal at SDB (Figure 6). The benthic  $\delta^{13}C$ , however, shows an increasing proximal-distal  $\delta^{13}C$  gradient, from the more up-dip SDB and WL sites to the more down-dip BR site. The relative proximity of the site to the paleo-shoreline and/or river mouth would suggest an enhanced terrestrial influence, resulting in lower  $\delta^{13}C$  values than deeper fully marine sites (Mackensen & Schmiedl, 2019; Stassen et al., 2012). The discrepancies between the  $\delta^{13}C_{\text{bulk}}$  and  $\delta^{13}C_{\text{benthic}}$  records, especially at WL and Millville could be due to uncertain contributions of fine fraction or detrital carbonate, or diagenetic effects (Zachos et al., 2005; Zachos & Arthur, 1986).

## 6 Paleotemperature evolution across the POE and PETM

Marine warming during the PETM ranges from average 5–8°C globally, depending on the environment, water depth and latitude (e.g. Dunkley Jones et al., 2013). TEX<sub>86</sub> temperatures from WL and BR (Sluijs, Brinkhuis, et al., 2007), as well as Mg/Ca and  $\delta^{18}$ O based upper water column temperatures (Babila et al., 2016), indicate a similar magnitude of rapid warming from the latest Paleocene to the PETM, followed by gradual cooling throughout the recovery phase. Paleocene bottom water temperatures at SDB average ~16–18°C and rise to at least to 20°C in the POE, though it should be noted that peak warming may not be fully captured given the dissolution horizon and lower resolution of the Mg/Ca data compared to  $\delta^{18}$ O. At SDB, a Mg/Ca-based temperature record shows a similar pattern with pre-POE temperatures of ~26–27°C in the upper water column and an overall temperature increase during the POE (~2°C, Babila et al., 2022). A TEX<sub>86</sub> and  $\delta^{18}$ O<sub>planktic+benthic</sub> based warming trend shortly predating the PETM is also observed in the data from WL and BR (Sluijs, Brinkhuis, et al., 2007; Zachos et al., 2006). The Mg/Ca of thermocline dwelling planktic foraminifera at BR shows a gradual, but relative to surface layers, delayed warming trend (Babila et al., 2016). Similar patterns have been observed in subtropical

619

620

621

622

623

624

625

626

627

628

629

630

631

632

633

634

635

636

637

638

639

640

641

642

643

644

645

646

and tropical sites (Tripati & Elderfield, 2004). Mixed layer temperatures above the PETM-dissolution interval at SDB reach values of 29–34°C during peak warming of the PETM (Babila et al., 2022) while bottom water temperatures reach 17–22°C. Bottom water temperatures from WL for this interval fluctuate around 26°C (in the assumption of a constant  $\delta^{18}O_{sw}$  of -0.5% across the PETM), with surface records reaching up to ~30–35°C (Zachos et al., 2006). During CIE recovery phase 1, the water column begins to cool until it reaches late Paleocene levels during CIE recovery phase 2. Overall bottom water Mg/Ca values at SDB are within the range, but commonly higher than equivalent global deep sea Mg/Ca records (Tripati & Elderfield, 2005).

As discussed above, an additional factor influencing  $\delta^{18}$ O values of marine carbonate is local salinity (or δ<sup>18</sup>O<sub>sw</sub>). Latest Paleocene benthic foraminiferal assemblages indicate a normal marine environment with stable salinity, and there is no evidence of nearshore influences on the benthic ecosystem In the CIE core phase, the environment is characterized by freshwater influx and stratification of the water column, but the benthic and planktic ecosystem indicate a continuation of marine conditions. The higher value might be an artefact of the low resolution of the Mg/Ca temperature record and the negative salinity influence on the Mg-incorporation in the foraminiferal tests. Culture and core-top studies on modern benthic foraminifera indicate no significant influence of seawater-pH on the Mg/Ca of the tests (Allison et al., 2010; Dissard et al., 2010; Rathmann & Kuhnert, 2008). δ<sup>18</sup>O increases with a decreased pH-level (Uchikawa & Zeebe, 2010), causing a possible underestimation of temperature and overestimation of salinity levels. Nonetheless, these results would suggest basin-wide freshening of the shelf, which seems in conflict with the relatively high abundances of marine planktic organisms (calcareous nannoplankton, planktic foraminifera; Self-Trail et al. 2012). On the other hand, far-reaching freshwater influx paired with a dense suspended sediment load can overcome the density boundary created by seawater and turn into a hyperpycnal flow or flow-events, transporting low-salinity waters to the bottom of the shelf (Mulder et al., 2003). Although the uncertainty in the magnitude of Asalinity is large, these findings would be consistent with climate model simulations of the PETM that show an increase in the frequency of heavy precipitation events which would trigger flooding and high energy fluvial events that can generate hyperpycnal flow (e.g. Carmichael et al., 2018; Rush et al., 2021).

#### 7 Conclusions

The SDB core provides an extensive and expanded record of the Paleocene-Eocene transition in which the latest Paleocene POE precedes the PETM, allowing for an in-depth analysis and comparison of the two CIEs. Both are characterized by a negative  $\delta^{13}$ C excursion (POE: ~2‰, PETM: ~4‰) and a shift to an overall finer grain-size. Using tie-points and sedimentation rates, we estimate the duration of the POE to be between 22 and 45 kyr and the duration between the upper boundary of the POE and the PETM to be between 80 and 100kyr. Due to the unlikelihood of constant sedimentation rates over such time spans, these estimates are highly uncertain.

The differing kaolinite content points to a POE sediment source (<5% kaolinite) that differs from the Marlboro Clay (>30% kaolinite) or is a result of mixing of sources, but a similar transport and deposition mechanism is not unlikely. The benthic foraminiferal assemblage differs significantly between the POE and the PETM. While some of the same stress-tolerant benthic taxa, which become dominant in the PETM, are present in the POE, they make up only a minor part of the assemblage (<5%). Taxa indicating oxygenated, oligotrophic bottom conditions are the dominant group in the late Paleocene interval, with stress tolerant taxa increasing in the uppermost part. Bottom water temperatures started to increase from the onset of the POE from ~17°C to ~19°C, followed by an acceleration of warming after the POE and reaching peak Paleocene values of 22°C. Our results indicate periodic changes in the hydrological cycle on, potentially, an eccentricity time scale and thus a less stable latest Paleocene climate state than previously realized.

The stratigraphic framework of the transition at SDB has been refined and adjusted based an integrated stratigraphy conflating isotopic, biological, ecological and lithological data and the subsequent correlation to sites nearby. The CIE core and recovery phase 1 are fully captured, whereas recovery phase 2 is only partially present in the SDB sequence, which is due to an unconformity truncating the top of the succession.

During the PETM, the sedimentation rate on the shelf increased by an order of magnitude (from <2.4 to <22.0 cm/kyr), as the Paleocene sediment-starved system changed to a river-dominated system, linked to an increased hydrological cycle on land. The increasingly stressful shelf environment – enhanced freshwater influx, decreased salinity, rising temperature and changes in food supply – is strongly reflected in the overall composition of benthic foraminiferal assemblages. Bottom waters eventually cooled and became better oxygenated with a stable food

supply, leading to gradual recovery of the shelf ecosystem to conditions similar to those of the late 677 Paleocene. 678 679 **Bibliography** 680 Alemán González, W. B., Powars, D. S., Seefelt, E. L., Edwards, L. E., Self-Trail, J. M., 681 Durand, C. T., et al. (2012). USGS Open-File Report 2012–1218: Preliminary physical 682 stratigraphy, biostratigraphy, and geophysical data of the USGS South Dover Bridge 683 684 core, Talbot County, Maryland (Open-File Report). South Dover Bridge, Talbot County, Maryland: USGS. Retrieved from https://pubs.usgs.gov/of/2012/1218/ 685 Allison, N., Austin, W., Paterson, D., & Austin, H. (2010). Culture studies of the benthic 686 687 foraminifera Elphidium williamsoni: Evaluating pH, Δ[CO32–] and inter-individual effects on test Mg/Ca. Chemical Geology, 274(1), 87–93. 688 https://doi.org/10.1016/j.chemgeo.2010.03.019 689 690 Alegret, L., Molina, E., & Thomas, E. (2003). Benthic foraminiferal turnover across the Cretaceous/Paleogene boundary at Agost (southeastern Spain): paleoenvironmental 691 inferences. Marine Micropaleontology, 48(3), 251–279. https://doi.org/10.1016/S0377-692 8398(03)00022-7 693 Babila, T. L., Rosenthal, Y., Wright, J. D., & Miller, K. G. (2016). A continental shelf 694 695 perspective of ocean acidification and temperature evolution during the Paleocene-Eocene Thermal Maximum. Geology, 44(4), 275–278. https://doi.org/10.1130/G37522.1 696 Babila, T. L., Penman, D. E., Hönisch, B., Kelly, D. C., Bralower, T. J., Rosenthal, Y., & 697 Zachos, J. C. (2018). Capturing the global signature of surface ocean acidification during 698 the Palaeocene–Eocene Thermal Maximum. Philosophical Transactions of the Royal 699

Society A: Mathematical, Physical and Engineering Sciences, 376(2130), 20170072. 700 701 https://doi.org/10.1098/rsta.2017.0072 Babila, T. L., Penman, D. E., Standish, C. D., Doubrawa, M., Bralower, T. J., Robinson, M. M., 702 703 et al. (2022). Surface ocean warming and acidification driven by rapid carbon release precedes Paleocene-Eocene Thermal Maximum. Science Advances, 8(11), eabg1025. 704 https://doi.org/10.1126/sciadv.abg1025 705 706 Bains, S., Corfield, R. M., & Norris, R. D. (1999). Mechanisms of climate warming at the end of 707 the Paleocene. Science, 285(5428), 724–727. https://doi.org/10.1126/science.285.5428.724 708 de Bar, M. W., de Nooijer, L. J., Schouten, S., Ziegler, M., Sluijs, A., & Reichart, G.-J. (2019). 709 710 Comparing Seawater Temperature Proxy Records for the Past 90 Myrs From the Shallow 711 Shelf Record Bass River, New Jersey. *Paleoceanography and Paleoclimatology*, 34(4), 712 455–475. https://doi.org/10.1029/2018PA003453 Bijl, P. K., Schouten, S., Sluijs, A., Reichart, G.-J., Zachos, J. C., & Brinkhuis, H. (2009). Early 713 714 Palaeogene temperature evolution of the southwest Pacific Ocean. *Nature*, 461(7265), 776–779. https://doi.org/10.1038/nature08399 715 Bornemann, A., Norris, R. D., Lyman, J. A., D'haenens, S., Groeneveld, J., Röhl, U., et al. 716 (2014). Persistent environmental change after the Paleocene–Eocene Thermal Maximum 717 in the eastern North Atlantic. Earth and Planetary Science Letters, 394, 70–81. 718 https://doi.org/10.1016/j.epsl.2014.03.017 719 Bowen, G. J., Maibauer, B. J., Kraus, M. J., Röhl, U., Westerhold, T., Steimke, A., et al. (2015). 720 Two massive, rapid releases of carbon during the onset of the Palaeocene–Eocene 721 722 thermal maximum. Nature Geoscience, 8(1), 44–47. https://doi.org/10.1038/ngeo2316

Boyle, E. A., & Keigwin, L. D. (1985). Comparison of Atlantic and Pacific paleochemical 723 724 records for the last 215,000 years: changes in deep ocean circulation and chemical inventories. Earth and Planetary Science Letters, 76(1), 135–150. 725 726 https://doi.org/10.1016/0012-821X(85)90154-2 Bralower, T. J., Kump, L. R., Self-Trail, J. M., Robinson, M. M., Lyons, S., Babila, T., et al. 727 (2018). Evidence for shelf acidification during the onset of the Paleocene-Eocene thermal 728 729 maximum. Paleoceanography and Paleoclimatology, 33. 730 https://doi.org/10.1029/2018PA003382 Carmichael, M. J., Pancost, R. D., & Lunt, D. J. (2018). Changes in the occurrence of extreme 731 precipitation events at the Paleocene–Eocene thermal maximum. Earth and Planetary 732 Science Letters, 501, 24–36. https://doi.org/10.1016/j.epsl.2018.08.005 733 734 Cramer, B. S., & Kent, D. V. (2005). Stable carbon isotope record of sediment core Ancora 735 [Data set]. Supplement to: Cramer, BS; Kent, DV (2005): Bolide summer: The Paleocene/Eocene thermal maximum as a response to an extraterrestrial trigger. 736 Palaeogeography, Palaeoclimatology, Palaeoecology. PANGAEA. 737 https://doi.org/10.1594/PANGAEA.824524 738 Cramer, B. S., Aubry, M.-P., Olsson, R. K., Miller, K. G., Wright, J. D., & Kent, D. V. (1999). 739 An exceptional chronologic, isotopic, and clay mineralogic record of the latest Paleocene 740 thermal maximum, Bass River, NJ, ODP 174AX. Bulletin de La Société Géologique de 741 France, 170(6), 883-897. 742 D'haenens, S., Bornemann, A., Stassen, P., & Speijer, R. P. (2012). Multiple early Eocene 743 benthic foraminiferal assemblage and δ13C fluctuations at DSDP Site 401 (Bay of Biscay — 744

NE Atlantic). Marine Micropaleontology, 88–89, 15–35. 745 https://doi.org/10.1016/j.marmicro.2012.02.006 746 Dissard, D., Nehrke, G., Reichart, G. J., & Bijma, J. (2010). Impact of seawater CO2on 747 748 calcification and Mg/Ca and Sr/Ca ratios in benthic foraminifera calcite: results from culturing experiments with Ammonia tepida. *Biogeosciences*, 7(1), 81–93. 749 https://doi.org/10.5194/bg-7-81-2010 750 Doubrawa, M., Stassen, P., Robinson, M. M., Babila, T. L., Zachos, J. C., & Speijer, R. P. 751 (2022). Shelf ecosystems along the U.S. Atlantic Coastal Plain prior to and during the 752 Paleocene-Eocene Thermal Maximum. [Dataset] PANGAEA. 753 https://doi.org/10.1594/PANGAEA.946947. 754 755 Dunkley Jones, T., Lunt, D. J., Schmidt, D. N., Ridgwell, A., Sluijs, A., Valdes, P. J., & Maslin, 756 M. (2013). Climate model and proxy data constraints on ocean warming across the Paleocene–Eocene Thermal Maximum. Earth-Science Reviews, 125, 123–145. 757 https://doi.org/10.1016/j.earscirev.2013.07.004 758 759 Elling, F. J., Gottschalk, J., Doeana, K. D., Kusch, S., Hurley, S. J., & Pearson, A. (2019). Archaeal lipid biomarker constraints on the Paleocene-Eocene carbon isotope excursion. 760 *Nature Communications*, 10(1), 4519. https://doi.org/10.1038/s41467-019-12553-3 761 Ernst, S. R., Guasti, E., Dupuis, C., & Speijer, R. P. (2006). Environmental perturbation in the 762 southern Tethys across the Paleocene/Eocene boundary (Dababiya, Egypt): Foraminiferal 763 and clay mineral records. Marine Micropaleontology, 60(1), 89–111. 764 https://doi.org/10.1016/j.marmicro.2006.03.002 765

Evans, D., & Müller, W. (2012). Deep time for aminifer a Mg/Ca paleothermometry: Nonlinear 766 767 correction for secular change in seawater Mg/Ca. Paleoceanography, 27(4). https://doi.org/10.1029/2012PA002315 768 769 Folk, R. L., & Ward, W. C. (1957). Brazos River bar [Texas]; a study in the significance of grain size parameters. Journal of Sedimentary Research, 27(1), 3–26. 770 https://doi.org/10.1306/74D70646-2B21-11D7-8648000102C1865D 771 772 Gibbs, S. J., Bown, P. R., Sessa, J. A., Bralower, T. J., & Wilson, P. A. (2006). Nannoplankton 773 extinction and origination across the Paleocene-Eocene Thermal Maximum. Science, 314(5806), 1770–1773. https://doi.org/10.1126/science.1133902 774 Gibson, T. G., & Bybell, L. M. (1991). Paleocoene-Eocene boundary sedimentation in the 775 Potomac river valley, Virginia and Maryland. I.G.C.P. Project 308 Field Trip Guidebook, 776 777 1-13.778 Gibson, T. G., Bybell, L. M., & Owens, J. P. (1993). Latest Paleocene lithologic and biotic 779 events in neritic deposits of southwestern New Jersey. *Paleoceanography*, 8(4), 495–514. https://doi.org/10.1029/93PA01367 780 Gibson, T. G., Bybell, L. M., & Mason, D. B. (2000). Stratigraphic and climatic implications of 781 clay mineral changes around the Paleocene/Eocene boundary of the northeastern US 782 margin. Sedimentary Geology, 134(1-2), 65-92. https://doi.org/10.1016/S0037-783 0738(00)00014-2 784 Gingerich, P. D. (2019). Temporal scaling of carbon emission and accumulation rates: Modern 785 anthropogenic emissions compared to estimates of PETM onset accumulation. 786 Paleoceanography and Paleoclimatology, 34(3), 329–335. 787 788 https://doi.org/10.1029/2018PA003379

Giusberti, L., Rio, D., Agnini, C., Backman, J., Fornaciari, E., Tateo, F., & Oddone, M. (2007). 789 Mode and tempo of the Paleocene-Eocene thermal maximum in an expanded section 790 from the Venetian pre-Alps. GSA Bulletin, 119(3–4), 391–412. 791 792 https://doi.org/10.1130/B25994.1 Hantsoo, K. G., Kump, L. R., Haupt, B. J., & Bralower, T. J. (2018). Tracking the Paleocene-793 Eocene Thermal Maximum in the North Atlantic: A shelf-to-basin analysis with a Regional 794 795 Ocean Model. Paleoceanography and Paleoclimatology. https://doi.org/10.1029/2018PA003371 796 Hines, B. R., Hollis, C. J., Atkins, C. B., Baker, J. A., Morgans, H. E. G., & Strong, P. C. (2017). 797 Reduction of oceanic temperature gradients in the early Eocene Southwest Pacific Ocean. 798 799 Palaeogeography, Palaeoclimatology, Palaeoecology, 475, 41–54. 800 https://doi.org/10.1016/j.palaeo.2017.02.037 801 Hollis, C. J., Dunkley Jones, T., Anagnostou, E., Bijl, P. K., Cramwinckel, M. J., Cui, Y., et al. (2019). The DeepMIP contribution to PMIP4: methodologies for selection, compilation 802 803 and analysis of latest Paleocene and early Eocene climate proxy data, incorporating version 0.1 of the DeepMIP database. Geoscientific Model Development, 12(7), 3149– 804 3206. https://doi.org/10.5194/gmd-12-3149-2019 805 Jackson, M. L. (2005). Soil chemical analysis: Advanced course, 2nd Ed. UW-Madison Libraries 806 Parallel Press. 807 John, C. M., Bohaty, S. M., Zachos, J. C., Sluijs, A., Gibbs, S., Brinkhuis, H., & Bralower, T. J. 808 (2008). North American continental margin records of the Paleocene-Eocene thermal 809 maximum: Implications for global carbon and hydrological cycling. Paleoceanography, 810 811 23(2). https://doi.org/10.1029/2007PA001465

812	John, C. M., Banerjee, N. R., Longstaffe, F. J., Sica, C., Law, K. R., & Zachos, J. C. (2012). Clay
813	assemblage and oxygen isotopic constraints on the weathering response to the Paleocene-
814	Eocene thermal maximum, east coast of North America. Geology, 40(7), 591-594.
815	https://doi.org/10.1130/G32785.1
816	Jones, S. M., Hoggett, M., Greene, S. E., & Jones, T. D. (2019). Large Igneous Province
817	thermogenic greenhouse gas flux could have initiated Paleocene-Eocene Thermal
818	Maximum climate change. Nature Communications, 10(1), 1–16.
819	https://doi.org/10.1038/s41467-019-12957-1
820	Kaiho, K. (1994). Benthic foraminiferal dissolved-oxygen index and dissolved-oxygen levels in
821	the modern ocean. Geology, 22(8), 719–722. https://doi.org/10.1130/0091-7613(1994)022
822	Kender, S., Stephenson, M. H., Riding, J. B., Leng, M. J., Knox, R. W. O., Peck, V. L., et al.
823	(2012). Marine and terrestrial environmental changes in NW Europe preceding carbon
824	release at the Paleocene-Eocene transition. Earth and Planetary Science Letters, 353-
825	354, 108–120. https://doi.org/10.1016/j.epsl.2012.08.011
826	Kennett, J. P., & Stott, L. D. (1991). Abrupt deep-sea warming, palaeoceanographic changes and
827	benthic extinctions at the end of the Palaeocene. Nature, 353(6341), 225-229.
828	https://doi.org/10.1038/353225a0
829	Koch, P. L., Zachos, J. C., & Gingerich, P. D. (1992). Correlation between isotope records in
830	marine and continental carbon reservoirs near the Palaeocene/Eocene boundary. Nature,
831	358(6384), 319–322. https://doi.org/10.1038/358319a0
832	Kopp, R. E., Schumann, D., Raub, T. D., Powars, D. S., Godfrey, L. V., Swanson-Hysell, N. L.,
833	et al. (2009). An Appalachian Amazon? Magnetofossil evidence for the development of a

834	tropical river-like system in the mid-Atlantic United States during the Paleocene-Eocene
835	thermal maximum. Paleoceanography, 24(4). https://doi.org/10.1029/2009PA001783
836	Kozdon, R., Kelly, D. C., Kitajima, K., Strickland, A., Fournelle, J. H., & Valley, J. W. (2013).
837	In situ $\delta 18O$ and Mg/Ca analyses of diagenetic and planktic foraminiferal calcite
838	preserved in a deep-sea record of the Paleocene-Eocene thermal maximum.
839	Paleoceanography, 28(3), 517-528. https://doi.org/10.1002/palo.20048
840	Kranner, M., Harzhauser, M., Beer, C., Auer, G., & Piller, W. E. (2022). Calculating dissolved
841	marine oxygen values based on an enhanced Benthic Foraminifera Oxygen Index. Scientific
842	Reports, 12(1), 1376. https://doi.org/10.1038/s41598-022-05295-8
843	Luciani, V., Giusberti, L., Agnini, C., Backman, J., Fornaciari, E., & Rio, D. (2007). The
844	Paleocene-Eocene Thermal Maximum as recorded by Tethyan planktonic foraminifera in
845	the Forada section (northern Italy). Marine Micropaleontology, 64(3), 189–214.
846	https://doi.org/10.1016/j.marmicro.2007.05.001
847	Lynch-Stieglitz, J., Curry, W. B., & Slowey, N. (1999). A geostrophic transport estimate for the
848	Florida Current from the oxygen isotope composition of benthic foraminifera.
849	Paleoceanography, 14(3), 360-373. https://doi.org/10.1029/1999PA900001
850	Lyons, S. L., Baczynski, A. A., Babila, T. L., Bralower, T. J., Hajek, E. A., Kump, L. R., et al.
851	(2019). Palaeocene–Eocene Thermal Maximum prolonged by fossil carbon oxidation.
852	Nature Geoscience, 12(1), 54. https://doi.org/10.1038/s41561-018-0277-3
853	Mackensen, A., & Schmiedl, G. (2019). Stable carbon isotopes in paleoceanography:
854	atmosphere, oceans, and sediments. Earth-Science Reviews, 197, 102893.
855	https://doi.org/10.1016/j.earscirev.2019.102893

856	Makarova, M., Wright, J. D., Miller, K. G., Babila, T. L., Rosenthal, Y., & Park, J. I. (2017).
857	Hydrographic and ecologic implications of foraminiferal stable isotopic response across
858	the U.S. mid-Atlantic continental shelf during the Paleocene-Eocene Thermal Maximum.
859	Paleoceanography, 32(1), 56-73. https://doi.org/10.1002/2016PA002985
860	Marchitto, T. M., Curry, W. B., Lynch-Stieglitz, J., Bryan, S. P., Cobb, K. M., & Lund, D. C.
861	(2014). Improved oxygen isotope temperature calibrations for cosmopolitan benthic
862	foraminifera. Geochimica et Cosmochimica Acta, 130, 1-11.
863	https://doi.org/10.1016/j.gca.2013.12.034
864	McInerney, F. A., & Wing, S. L. (2011). The Paleocene-Eocene Thermal Maximum: A
865	perturbation of carbon cycle, climate, and biosphere with implications for the future.
866	Annual Review of Earth and Planetary Sciences, 39(1), 489–516.
867	https://doi.org/10.1146/annurev-earth-040610-133431
868	Miller, K. G. (Ed.). (1999). Proceedings of the Ocean Drilling Program, Initial reports, Volume
869	174AX (Suppl.): College Station, TX, Ocean Drilling Program "Sandy Hook Sites."
870	Ocean Drilling Program. https://doi.org/10.2973/odp.proc.ir.174AXS.1999
871	Mulder, T., Syvitski, J. P. M., Migeon, S., Faugères, JC., & Savoye, B. (2003). Marine
872	hyperpycnal flows: initiation, behavior and related deposits. A review. Marine and
873	Petroleum Geology, 20(6), 861–882. https://doi.org/10.1016/j.marpetgeo.2003.01.003
874	Murphy, B. H., Farley, K. A., & Zachos, J. C. (2010). An extraterrestrial 3He-based timescale
875	for the Paleocene-Eocene thermal maximum (PETM) from Walvis Ridge, IODP Site
876	1266. Geochimica et Cosmochimica Acta, 74(17), 5098–5108.
877	https://doi.org/10.1016/j.gca.2010.03.039

878	Nguyen, T. M. P., Petrizzo, M. R., & Speijer, R. P. (2009). Experimental dissolution of a fossil
879	foraminiferal assemblage (Paleocene-Eocene Thermal Maximum, Dababiya, Egypt):
880	Implications for paleoenvironmental reconstructions. Marine Micropaleontology, 73(3-
881	4), 241–258. https://doi.org/10.1016/j.marmicro.2009.10.005
882	Nogan, D. S. (1964). Foraminifera, stratigraphy, and paleoecology of the Aquia Formation of
883	Maryland and Virginia (Vol. Sepcial Publication 7). Cushman Foundation for
884	Foraminiferal Research. Retrieved from
885	http://catalog.hathitrust.org/api/volumes/oclc/1101776.html
886	Rathmann, S., & Kuhnert, H. (2008). Carbonate ion effect on Mg/Ca, Sr/Ca and stable isotopes
887	on the benthic foraminifera Oridorsalis umbonatus off Namibia. Marine
888	Micropaleontology, 66(2), 120–133. https://doi.org/10.1016/j.marmicro.2007.08.001
889	Robinson, M. M., & Spivey, W. E. (2019). Environmental and geomorphological changes on the
890	eastern North American continental shelf across the Paleocene-Eocene boundary.
891	Paleoceanography and Paleoclimatology, 34(4), 715–732.
892	https://doi.org/10.1029/2018PA003357
893	Röhl, U., Westerhold, T., Bralower, T. J., & Zachos, J. C. (2007). On the duration of the
894	Paleocene-Eocene thermal maximum (PETM). Geochemistry, Geophysics, Geosystems,
895	8(12). https://doi.org/10.1029/2007GC001784
896	Rosenthal, Y., Boyle, E. A., & Slowey, N. (1997). Temperature control on the incorporation of
897	magnesium, strontium, fluorine, and cadmium into benthic foraminiferal shells from
898	Little Bahama Bank: Prospects for thermocline paleoceanography. Geochimica et
899	Cosmochimica Acta, 61(17), 3633–3643. https://doi.org/10.1016/S0016-7037(97)00181-
900	6

Rostami, M. A., Frontalini, F., Leckie, R. M., Coccioni, R., Font, E., & Balmaki, B. (2020). 901 902 Benthic foraminifera across the Cretaceous/Paleogene boundary in the Eastern Tethys (Northern Alborz, Galanderud Section): Extinction pattern and paleoenvironmental 903 904 reconstruction. Journal of Foraminiferal Research, 50(1), 25–40. https://doi.org/10.2113/gsjfr.50.1.25 905 Rush, W. D., Kiehl, J. T., Shields, C. A., & Zachos, J. C. (2021). Increased frequency of extreme 906 907 precipitation events in the North Atlantic during the PETM: Observations and theory. Palaeogeography, Palaeoclimatology, Palaeoecology, 568, 110289. 908 https://doi.org/10.1016/j.palaeo.2021.110289 909 Self-Trail, J. M. (2011). Paleogene calcareous nannofossils of the South Dover Bridge core, 910 911 Southern Maryland (USA). *Journal of Nannoplankton Research*, 32(1), 1–28. 912 Self-Trail, J. M., Powars, D. S., Watkins, D. K., & Wandless, G. A. (2012). Calcareous 913 nannofossil assemblage changes across the Paleocene–Eocene Thermal Maximum: Evidence from a shelf setting. *Marine Micropaleontology*, 92–93, 61–80. 914 915 https://doi.org/10.1016/j.marmicro.2012.05.003 Self-Trail, J. M., Robinson, M., J. Bralower, T., Sessa, J., A. Hajek, E., Kump, L., et al. (2017). 916 Shallow marine response to global climate change during the Paleocene-Eocene Thermal 917 Maximum, Salisbury Embayment, USA: PETM coastal response. *Paleoceanography*. 918 919 https://doi.org/10.1002/2017PA003096 920 Sluijs, A., Schouten, S., Pagani, M., Woltering, M., Brinkhuis, H., Damsté, J. S. S., et al. (2006). Subtropical Arctic Ocean temperatures during the Palaeocene/Eocene thermal maximum. 921 *Nature*, 441(7093), 610–613. https://doi.org/10.1038/nature04668 922

923	Sluijs, A., Brinkhuis, H., Schouten, S., Bohaty, S. M., John, C. M., Zachos, J. C., et al. (2007).
924	Environmental precursors to rapid light carbon injection at the Palaeocene/Eocene
925	boundary. Nature, 450(7173), 1218–1221. https://doi.org/10.1038/nature06400
926	Sluijs, A., Bowen, G. J., Brinkhuis, H., Lourens, L. J., & Thomas, E. (2007). The Palaeocene-
927	Eocene Thermal Maximum super greenhouse: biotic and geochemical signatures, age
928	models and mechanisms of global change. Deep-Time Perspectives on Climate Change:
929	Marrying the Signal from Computer Models and Biological Proxies, 323–349.
930	https://doi.org/10.1144/TMS002.15
931	Sluijs, A., Brinkhuis, H., Crouch, E. M., John, C. M., Handley, L., Munsterman, D., et al. (2008).
932	Eustatic variations during the Paleocene-Eocene greenhouse world. Paleoceanography,
933	23(4). https://doi.org/10.1029/2008PA001615
934	Speijer, R. P., Van der Zwaan, G. J., & Schmitz, B. (1996). The impact of Paleocene/Eocene
935	boundary events on middle neritic benthic foraminiferal assemblages from Egypt. Marine
936	Micropaleontology, 28(2), 99-132. https://doi.org/10.1016/0377-8398(95)00079-8
937	Speijer, R. P., & Schmitz, B. (1998). A benthic foraminiferal record of Paleocene sea level and
938	trophic/redox conditions at Gebel Aweina, Egypt. Palaeogeography, Palaeoclimatology,
939	Palaeoecology, 137(1), 79–101. https://doi.org/10.1016/S0031-0182(97)00107-7
940	Speijer, R. P., & Wagner, T. (2002). Sea-level changes and black shales associated with the late
941	Paleocene thermal maximum: Organic-geochemical and micropaleontologic evidence
942	from the southern Tethyan margin (Egypt-Israel), 356, 533-549.
943	https://doi.org/10.1130/0-8137-2356-6.533
944	Speijer, R. P., Scheibner, C., Stassen, P., & Morsi, AM. M. (2012). Response of marine
945	ecosystems to deep-time global warming: a synthesis of biotic patterns across the

946	Paleocene-Eocene thermal maximum (PETM). Austrian Journal of Earth Sciences,
947	<i>105</i> (1), 6–16.
948	Stassen, P. (2012). The impact of the Paleocene-Eocene Thermal Maximum on benthic
949	foraminiferal shelf communities (PhD thesis). KU Leuven, Leuven.
950	Stassen, P., Thomas, E., & Speijer, R. (2009). Benthic foraminiferal isotope records across the
951	PETM from the New Jersey Coastal Plain. In Climatic and Biotic Events of the
952	Paleogene, Extended abstracts from an international conference (Vol. 18, pp. 135–137).
953	Institute of Geological and Nuclear Sciences Limited; Lower Hutt, New Zealand.
954	Retrieved from https://lirias.kuleuven.be/retrieve/121061
955	Stassen, P., Thomas, E., & Speijer, R. P. (2012). Integrated stratigraphy of the Paleocene-Eocene
956	thermal maximum in the New Jersey Coastal Plain: Toward understanding the effects of
957	global warming in a shelf environment. Paleoceanography, 27.
958	https://doi.org/10.1029/2012PA002323
959	Stassen, P., Thomas, E., & Speijer, R. P. (2015). Paleocene-Eocene Thermal Maximum
960	environmental change in the New Jersey Coastal Plain: benthic foraminiferal biotic
961	events. <i>Marine Micropaleontology</i> , 115, 1–23.
962	https://doi.org/10.1016/j.marmicro.2014.12.001
963	Thomas, D. J., Zachos, J. C., Bralower, T. J., Thomas, E., & Bohaty, S. (2002). Warming the
964	fuel for the fire: Evidence for the thermal dissociation of methane hydrate during the
965	Paleocene-Eocene thermal maximum. Geology, 30(12), 1067–1070.
966	https://doi.org/10.1130/0091-7613(2002)030<1067:WTFFTF>2.0.CO;2
967	Thomas, E. (1998). Biogeography of the Late Paleocene benthic foraminiferal extinction. In Late
968	Paleocene-early Eocene biotic and climatic events in the marine and terrestrial records

969	(pp. 214–243). New York: Columbia University Press. Retrieved from
970	https://digitalcollections.wesleyan.edu/object/eesfp-43
971	Thomas, E., & Shackleton, N. J. (1996). The Paleocene-Eocene benthic foraminiferal extinction
972	and stable isotope anomalies. Geological Society, London, Special Publications, 101,
973	401–441.
974	Trampush, S. M., & Hajek, E. A. (2017). Preserving proxy records in dynamic landscapes:
975	Modeling and examples from the Paleocene-Eocene Thermal Maximum. Geology,
976	45(11), 967–970. https://doi.org/10.1130/G39367.1
977	Tripati, A., & Elderfield, H. (2004). Abrupt hydrographic changes in the equatorial Pacific and
978	subtropical Atlantic from foraminiferal Mg/Ca indicate greenhouse origin for the therma
979	maximum at the Paleocene-Eocene boundary. Geochemistry, Geophysics, Geosystems,
980	5(2). https://doi.org/10.1029/2003GC000631
981	Tripati, A., & Elderfield, H. (2005). Deep-sea temperature and circulation changes at the
982	Paleocene-Eocene Thermal Maximum. Science, 308(5730), 1894–1898.
983	https://doi.org/10.1126/science.1109202
984	Uchikawa, J., & Zeebe, R. E. (2010). Examining possible effects of seawater pH decline on
985	foraminiferal stable isotopes during the Paleocene-Eocene Thermal Maximum.
986	Paleoceanography, 25(2). https://doi.org/10.1029/2009PA001864
987	Westerhold, T., Marwan, N., Drury, A. J., Liebrand, D., Agnini, C., Anagnostou, E., et al.
988	(2020). An astronomically dated record of Earth's climate and its predictability over the
989	last 66 million years. Science, 369(6509), 1383–1387.
990	https://doi.org/10.1126/science.aba6853

991	Zachos, J. C., & Arthur, M. A. (1986). Paleoceanography of the Cretaceous/Tertiary boundary
992	event: Inferences from stable isotopic and other data. <i>Paleoceanography</i> , <i>I</i> (1), 5–26.
993	https://doi.org/10.1029/PA001i001p00005
994	Zachos, J. C., Röhl, U., Schellenberg, S. A., Sluijs, A., Hodell, D. A., Kelly, D. C., et al. (2005)
995	Rapid acidification of the ocean during the Paleocene-Eocene thermal maximum.
996	Science, 308(5728), 1611-1615. https://doi.org/10.1126/science.1109004
997	Zachos, J. C., Schouten, S., Bohaty, S., Quattlebaum, T., Sluijs, A., Brinkhuis, H., et al. (2006).
998	Extreme warming of mid-latitude coastal ocean during the Paleocene-Eocene Thermal
999	Maximum: Inferences from TEX86 and isotope data. Geology, 34.
1000	https://doi.org/10.1130/G22522.1
1001	Zachos, J. C., Dickens, G. R., & Zeebe, R. E. (2008). An early Cenozoic perspective on
1002	greenhouse warming and carbon cycle dynamics. <i>Nature</i> , 451, 279–83.
1003	https://doi.org/10.1038/nature06588
1004	Zeebe, R. E., & Lourens, L. J. (2019). Solar system chaos and the Paleocene–Eocene boundary
1005	age constrained by geology and astronomy. Science, 365(6456), 926-929.
1006	https://doi.org/10.1126/science.aax0612
1007	Zeebe, R. E., Ridgwell, A., & Zachos, J. C. (2016). Anthropogenic carbon release rate
1008	unprecedented during the past 66 million years. <i>Nature Geoscience</i> , 9(4), 325–329.
1009	https://doi.org/10.1038/ngeo2681
1010	van der Zwaan, G. J., Jorissen, F. J., & de Stigter, H. C. (1990). The depth dependency of
1011	planktonic/benthic foraminiferal ratios: Constraints and applications. Marine Geology,
1012	95(1), 1–16. https://doi.org/10.1016/0025-3227(90)90016-D

van der Zwaan, G. J., Duijnstee, I. A. P., den Dulk, M., Ernst, S. R., Jannink, N. T., & 1013 Kouwenhoven, T. J. (1999). Benthic foraminifers: proxies or problems?: A review of 1014 paleocological concepts. Earth-Science Reviews, 46(1), 213–236. 1015 1016 https://doi.org/10.1016/S0012-8252(99)00011-2 1017 Acknowledgements 1018 1019 Financial support was provided by FWO (12D6717N) to PS, KU Leuven Research Fund (C14/17/057) to RPS and PS, and NSF (OCE-1415958) to JCZ. MMR was funded by the USGS 1020 1021 Climate Research and Development Program. Any use of trade, firm, or product names is for descriptive purposes only and does not imply endorsement by the U.S. Government. We kindly 1022 thank Rieko Adriaens (Q-mineral) for the clay mineralogy model. We also thank Lore Fondu 1023 (grain-size analysis), Linde Vanlook (lab), Oliver A. Kern (R-support), Edward Ballaron (trace-1024 1025 metal analyses), and Colin Carney (isotope analyses). We thank Tom Dunkley Jones and two 1026 anonymous reviewers for constructive reviews. 1027 1028 **Open Research** 1029 Samples are identified by the abbreviation of the drill core (SDB) and depth below surface in 1030 meter. All data used in the study are openly available at PANGAEA via (Doubrawa et al. 2022).

## **Figure captions**

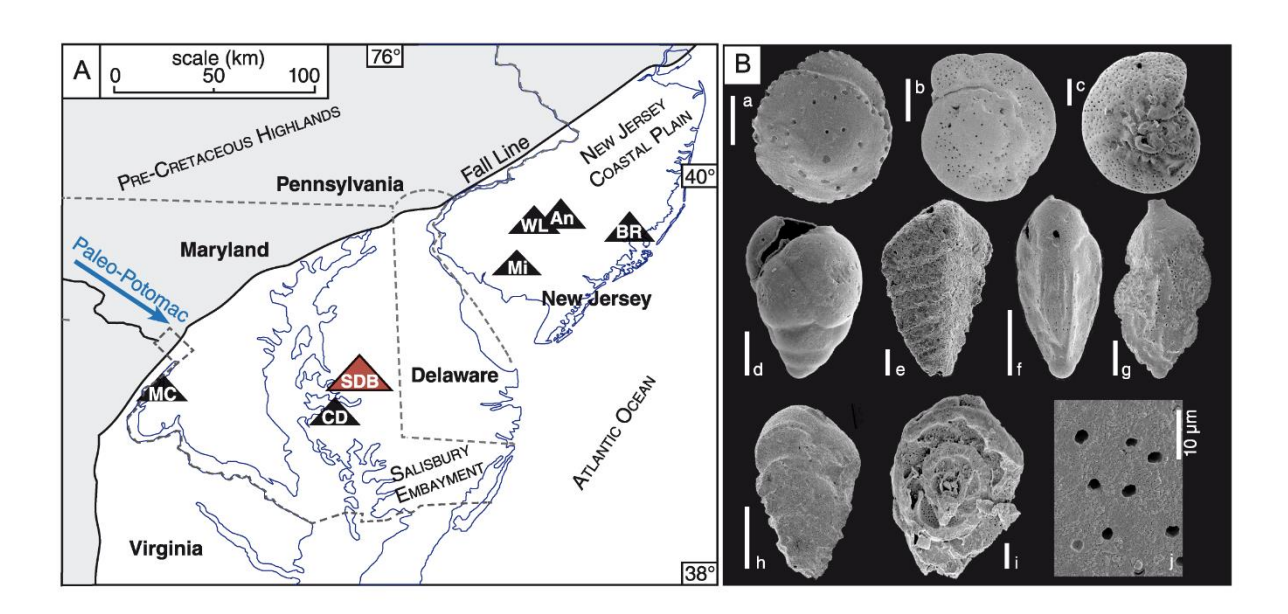


Figure 1A: Locations of core-sites (modified after Stassen et al., 2012). Site abbreviations: An = Ancora, BR = Bass River, CD = CamDor, MC = Mattawoman Creek-Billingsley Road, Mi = Millville, SDB = South Dover Bridge, WL = Wilson Lake.

1B: Scanning electron microscope (SEM) images of benthic foraminifera from SDB, scale bar represents 50 μm. a: Pulsiphonina prima (202.24 m), b: Cibicidoides alleni (208.96 m), c: Anomalinoides acutus (196.15 m), d: Turrilina brevispira (204.48 m), e: Spiroplectinella laevis (189.57 m), f: Bulimina virginiana (189,57 m), g: Pseudouvigerina triangularis (197.16 m), h: Tappanina selmensis (191.03), i: inside of a Cibicidoides alleni test (207.02 m), j: detail of outer test wall of Cibicidoides alleni (204.48 m).

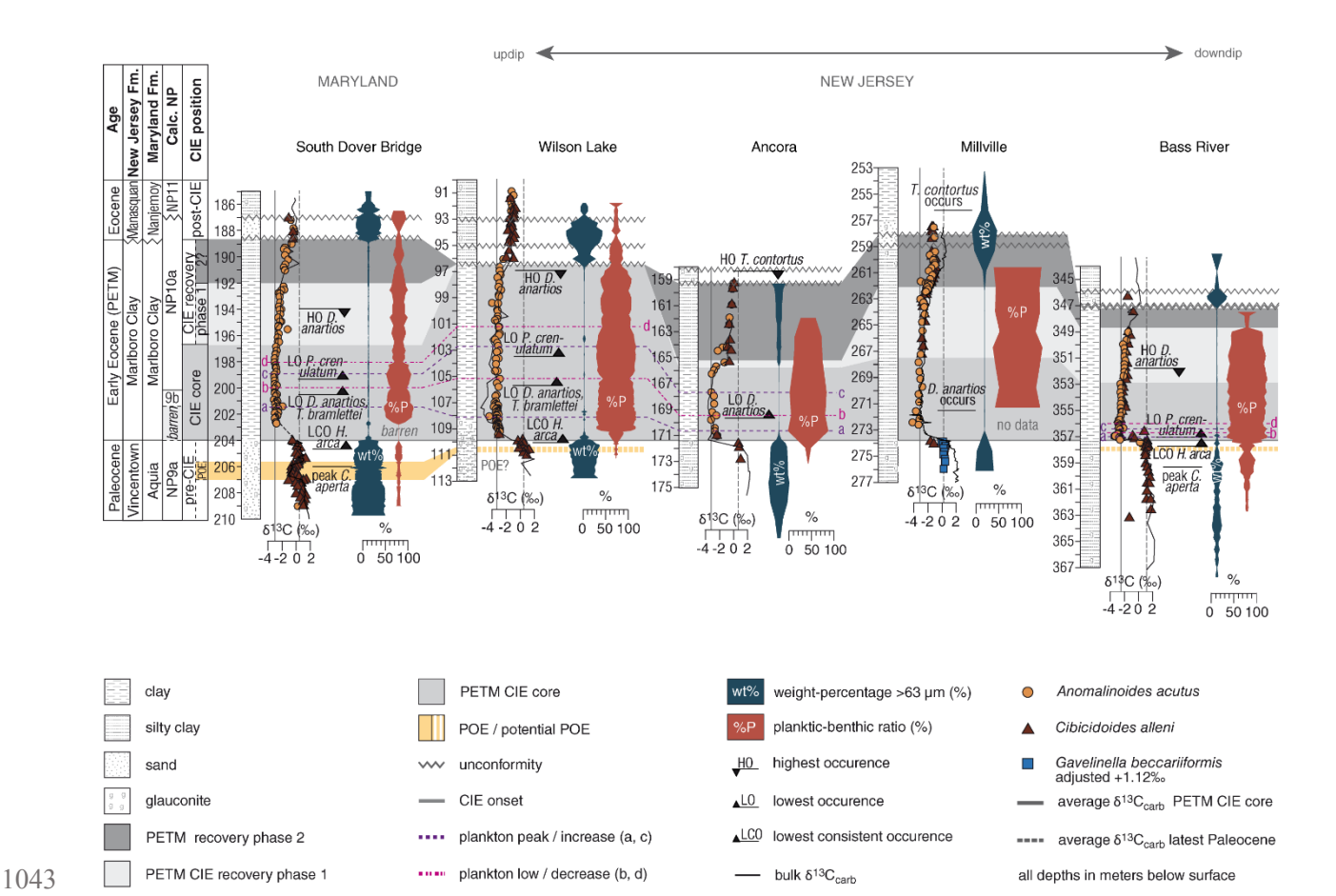


Figure 2: Stratigraphic correlation along the U.S. Atlantic Coastal Plain based on δ<sup>13</sup>C<sub>benthic+bulk</sub> (‰), weight percentage of the >63 μm fraction (wt%, blue violin plot), planktic-benthic ratio (%P, red violin plot) and nannoplankton biostratigraphy. CIE subdivision following Röhl et al. (2007) and recovery phase estimates.

Paleocene δ<sup>13</sup>C<sup>benthic</sup> values of Gavelinella beccariiformis from the Millville core are adjusted to Cibicidoides alleni and Anomalinoides acutus values by the correction factor 1.12‰ (Stassen, 2012; Stassen et al., 2009). Data sources: South Dover Bridge (this study; Babila et al., 2022; Self-Trail, 2011), WL (Gibbs et al., 2006; Stassen et al., 2012; Zachos et al., 2006), Ancora (Cramer & Kent, 2005; Harris, 2010; Harris et al., 2010; Kent et al., 2003; Miller, 1999), Millville (Harris, 2010; Harris et al., 2010; Makarova et al., 2017; Sugarman et al., 2005; Wright & Schaller, 2013), BR (Cramer et al., 1999; Gibbs et al., 2006; John et al., 2008; Kent et al., 2003; Stassen et al., 2012).

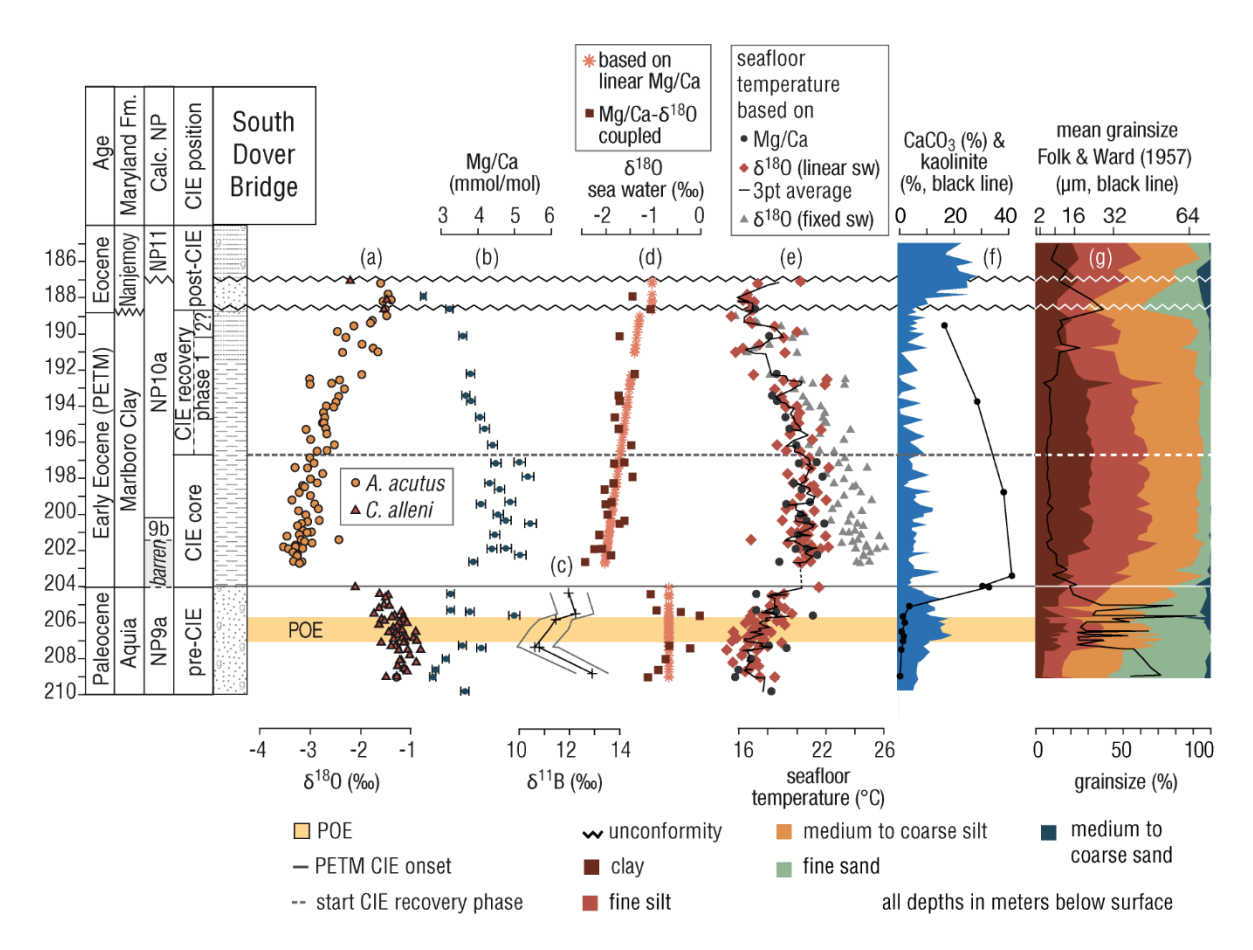


Figure 3: South Dover Bridge: (a)  $\delta^{18}O_{foram}$  (%); (b) Mg/Ca (mmol/mol) with 3% error bars (based on benthic foraminifera, Paleocene: Cibicidoides alleni, PETM: Anomalinoides acutus); (c)  $\delta^{11}B$  (%) and error interval (grey lines, (Babila et al., 2022)); (d) calculated seawater  $\delta^{18}O$  (%); (e) seafloor temperature estimates (°C) based on Mg/Ca,  $\delta^{18}O$  with a linear  $\delta^{18}O_{sw}$  (red diamonds, linear trend derived from coupling of the Mg/Ca with the  $\delta^{18}O_{foram}$  data) and with a fixed  $\delta^{18}O_{sw}$  of -1.2% for the PETM interval (grey triangles); (f) CaCO<sub>3</sub> content (%) and kaolinite content (% of whole clay suite – black line); (g) gGrain-size distributions (%) based on Laser Diffraction Particle Size Analyses and mean grain-size based on Folk & Ward (1957, black line in  $\mu$ m).

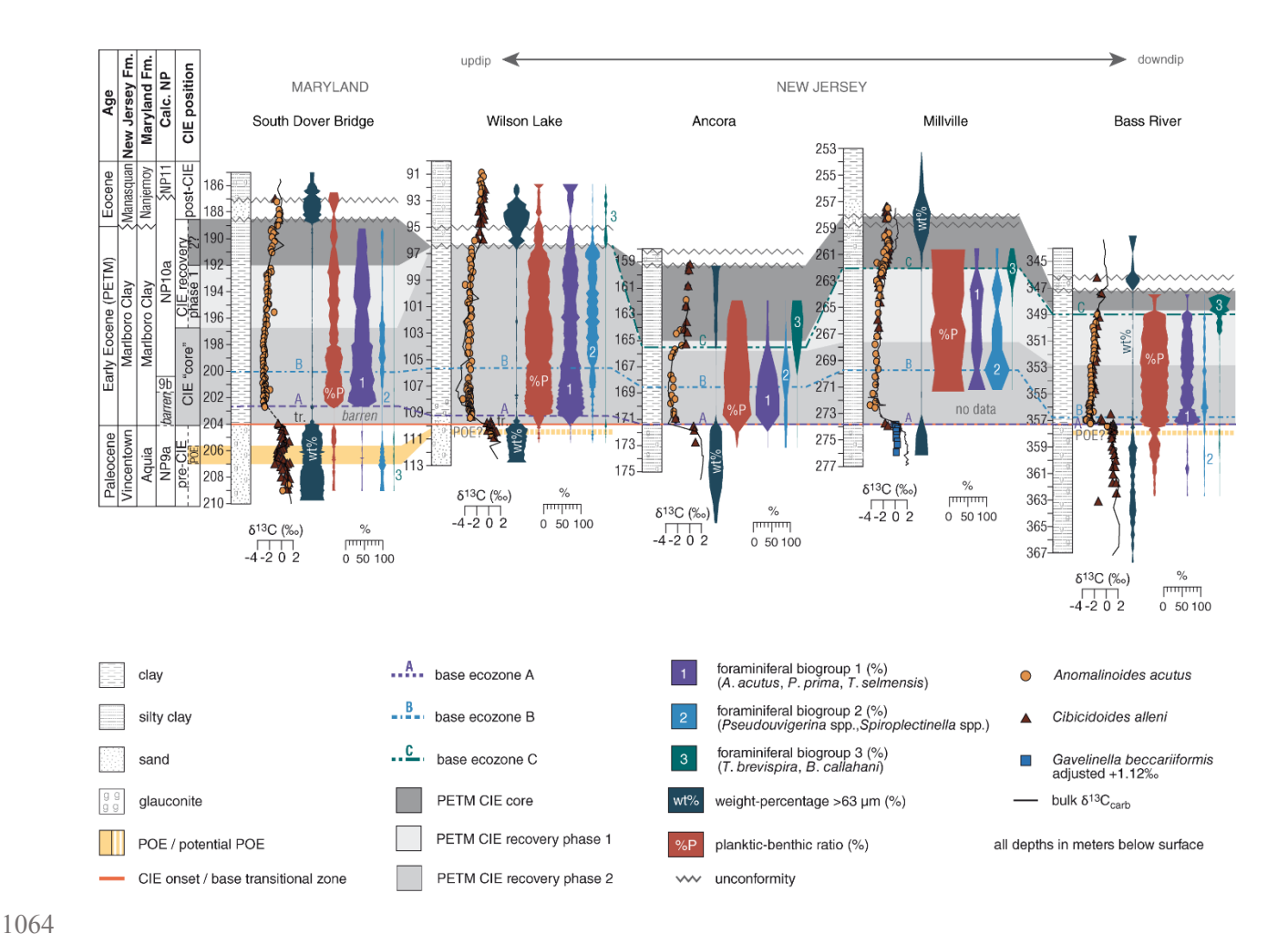


Figure 4: Stratigraphic correlation of Paleocene-Eocene sections along the U.S. Coastal Plain based on  $\delta^{13}C_{benthic+bulk}$  (%), weight percentage of the fraction >63  $\mu$ m (wt%, blue violin plot), planktic-benthic ratio (%P, red violin plot)), and distribution patterns of biogroups 1–3 (plotted as percentage of whole benthic foraminiferal assemblage) based on Stassen et al. (2012). Paleocene  $\delta^{13}C_{benthic}$  values of Gavelinella beccariiformis from the Millville core are adjusted to Cibicidoides alleni and Anomalinoides acutus values by the correction factor 1.12% (Stassen, 2012; Stassen et al., 2009). Sources of foraminiferal assemblage data: South Dover Bridge (this study), WL and BR (Stassen et al., 2012), Ancora and Millville (Harris, 2010).

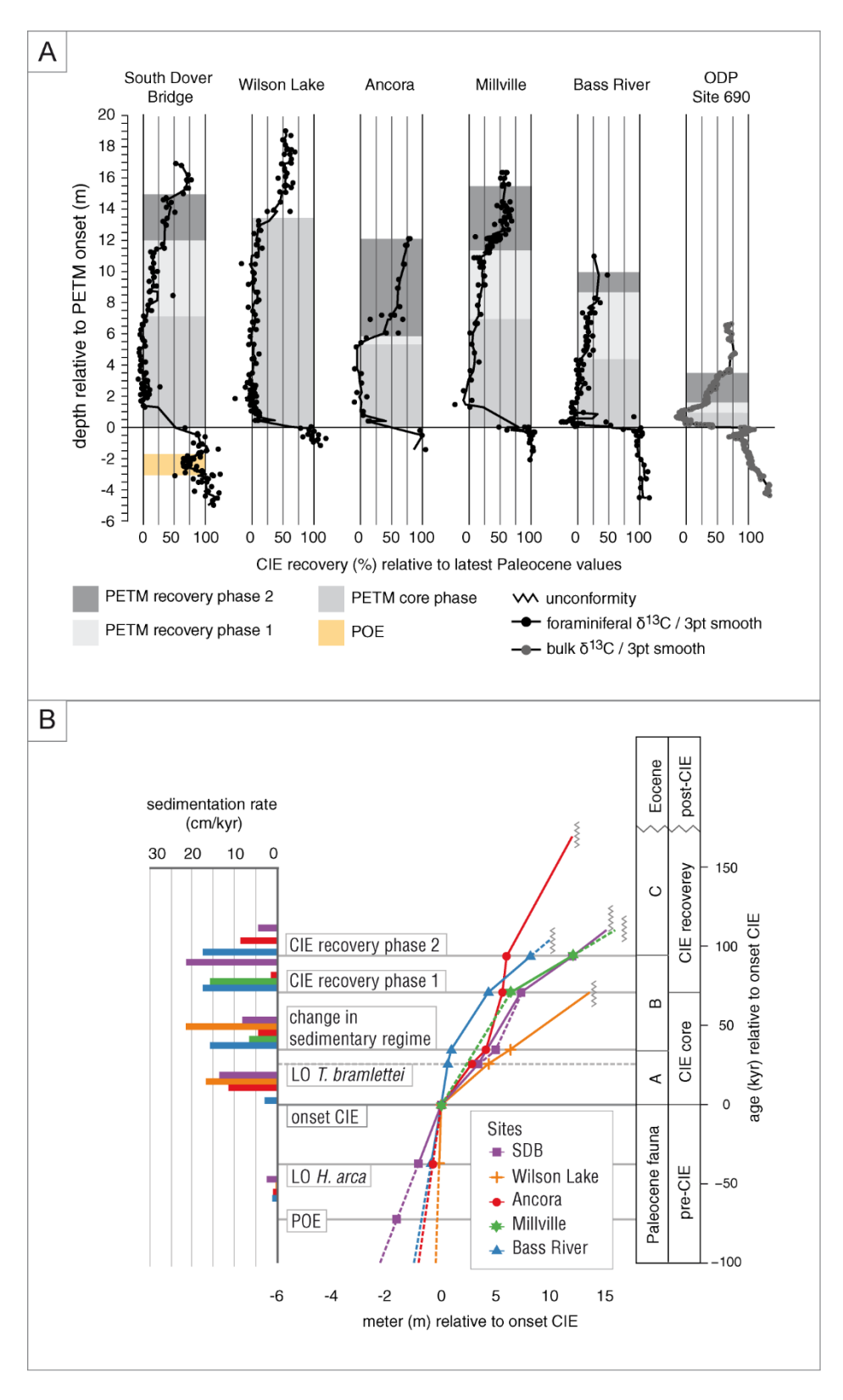
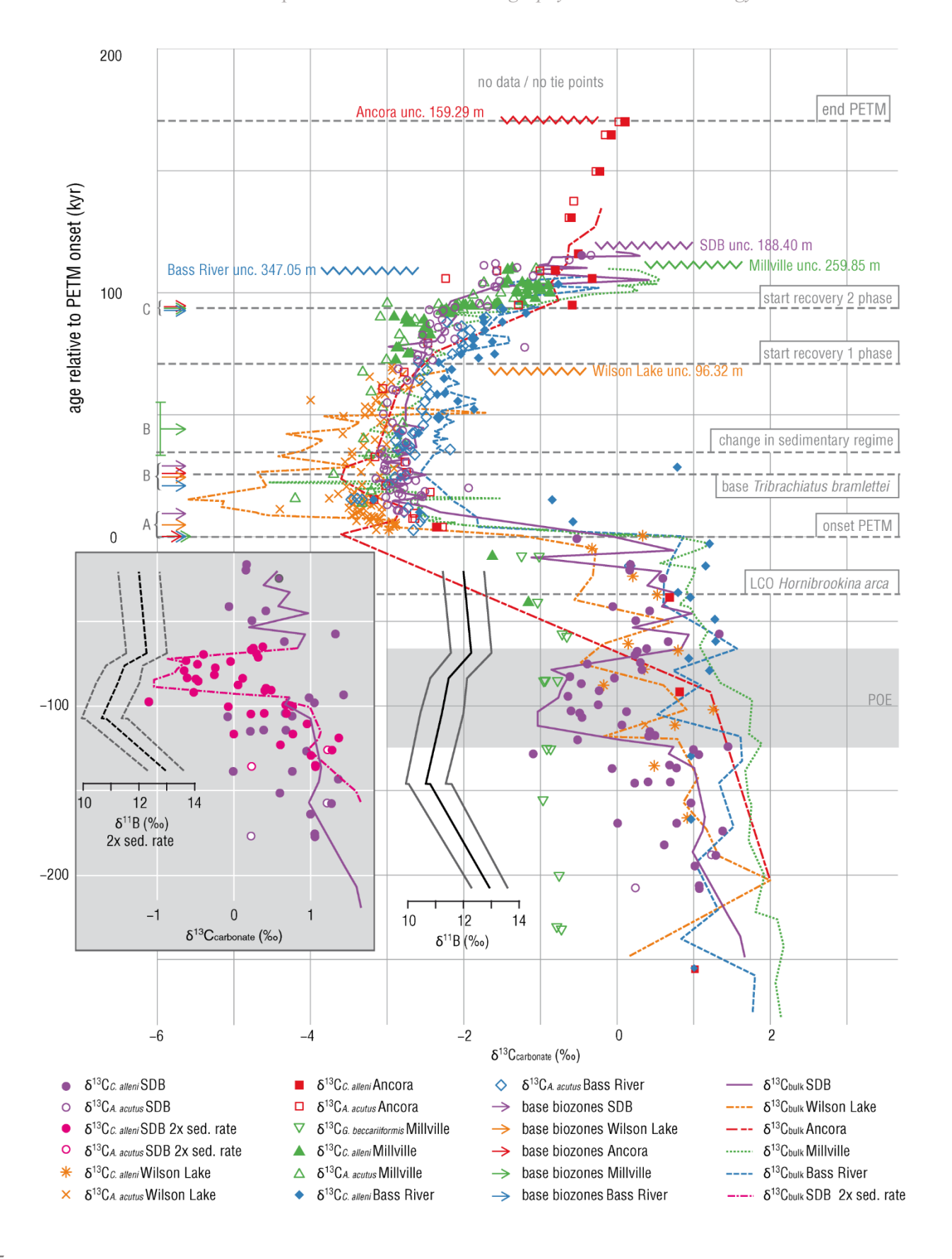


Figure 5A: Progression of CIE recovery phases based on  $\delta^{13}C_{benthic}$  (Anomalinoides acutus, Cibicidoides alleni, Gavelinella beccariiformis) from the shallow shelf sites SDB, Ancora, BR, Millville, and WL and Southern Ocean

## manuscript submitted to Paleoceanography and Paleoclimatology

1076	ODP Site 690 Maud Rise (bulk data, data sources are as indicated in caption of Figure 3, for ODP site 690: Bains
1077	et al., 1999). Reaching Paleocene $\delta_{13}C$ values (excluding POE data), is considered a 100% recovery. Gavelinella
1078	beccariiformis in the Millville record is adjusted to C. alleni values by +1.12% (Stassen, 2012). Peak CIE levels are
1079	based on the interval between the lower two %P peaks after the PETM onset (Figure 3).
1080	5B: Depth-time plot and sedimentation rates based on the relative position and cyclostratigraphic ages of the CIE
1081	tie points (Röhl et al., 2007), the lowest common occurrence of Hornibrookina arca (extrapolated from BR), the
1082	lowest occurrence of Tribrachiatus bramlettei (Agnini et al., 2007) and the change in sedimentary regime (Stassen et
1083	al., 2012). Dashed lines indicate extrapolated sedimentation rates.
1084	



## manuscript submitted to Paleoceanography and Paleoclimatology

Figure 6:. Comparison of marine  $\delta^{13}C_{benthic+bulk}$  records (Cibicidoides alleni, Anomalinoides acutus, Gavelinella beccariiformis) from New Jersey and Maryland sites.  $\delta^{13}C$  records are plotted against a new and refined age model (this study), and Paleocene age estimates are based on sedimentation rates (Table 1). Paleocene Millville sedimentation rate assumed as 1 cm/kyr. Bases of ecozones A, B and C are indicated by arrows. Data sources as in caption of Figure 2. An alternative sedimentation rate for the POE at SDB is given in the inset grey box. Pink lines and dots indicate  $\delta^{13}C_{benthic+bulk}$  for a doubling of the sedimentation rate to 4.8 cm/kyr up until the top of the POE, purple dots if sedimentation rate pre- and post-POE is presumed as 2.4 cm/kyr. Black lines indicate the  $\delta^{11}B$  peak with error interval (grey lines, Babila et al., 2022), with doubled sedimentation rate in the grey box (dashed lines).